Atmospheric
Chemistry
and Physics

Laboratory studies of ice nucleation onto bare and internally mixed soot–sulfuric acid particles

Kunfeng Gao[1,2,3]**, Chong-Wen Zhou**[1]**, Eszter J. Barthazy Meier**[4]**, and Zamin A. Kanji**[3]

[1]School of Energy and Power Engineering, Beihang University, Beijing, China
[2]Shenyuan Honours College of Beihang University, Beihang University, Beijing, China
[3]Department of Environmental Systems Science, Institute for Atmospheric and Climate Science,
ETH Zurich, 8092 Zurich, Switzerland
[4]Scientific Centre for Optical and Electron Microscopy, ETH Zurich, 8093 Zurich, Switzerland

Correspondence: Zamin A. Kanji (zamin.kanji@env.ethz.ch) and Kunfeng Gao (gaokunfeng@buaa.edu.cn)

Abstract. Soot particles are potential candidates for ice-nucleating particles in cirrus cloud formation, which is known to exert a net-warming effect on climate. Bare soot particles, generally hydrophobic and fractal ones, mainly exist near emission sources. Coated or internally mixed soot particles are more abundant in the atmosphere and have a higher probability of impacting cloud formation and climate. However, the ice nucleation ability of coated soot particles is not as well understood as that of freshly produced soot particles. In this laboratory study, two samples, a propane flame soot and a commercial carbon black, were used as atmospheric soot surrogates and coated with varying wt % of sulfuric acid (H_2SO_4). The ratio of coating material mass to the mass of bare soot particles was controlled and progressively increased from less than 5 wt % to over 100 wt %. Both bare and coated soot particle ice nucleation activities were investigated with a continuous-flow diffusion chamber operated at mixed-phase and cirrus cloud conditions. The mobility diameter and mass distribution of size-selected soot particles with/without H_2SO_4 coating were measured by a scanning mobility particle sizer and a centrifugal particle mass analyser running in parallel. The mixing state and morphology of soot particles were characterized by scanning electron microscopy and transmission electron microscopy. In addition, the evidence of the presence of H_2SO_4 on a coated soot particle surface is shown by energy-dispersive X-ray spectroscopy. Our study demonstrates that H_2SO_4 coatings suppress the ice nucleation activity of soot particles to varying degrees depending on the coating thickness, but in a non-linear fashion. Thin coatings causing pore filling in the soot aggregate inhibits pore condensation and freezing. Thick coatings promote particle ice activation via droplet homogeneous freezing. Overall, our findings reveal that H_2SO_4 coatings will suppress soot particle ice nucleation abilities in the cirrus cloud regime, having implications for the fate of soot particles with respect to cloud formation in the upper troposphere.

1 Introduction

Black carbon (BC) particles associated with organics are called soot (Bond et al., 2013). Soot particles are of significance in both physical and chemical atmospheric processes in the atmosphere. In particular, these carbonaceous aerosol particles can engage in cloud formation processes and form hydrometeors, which affects their life cycle in the atmosphere and is the source of uncertainties about their overall climate impacts (Liu et al., 2020; Hu et al., 2021). A study estimated that 7.5 Mt BC was emitted into the atmosphere in the year 2000 globally with an uncertainty larger than 26.7 % (Bond et al., 2013). Lee et al. (2020) reported that aviation emission makes an important global contribution to anthropogenic climate forcing. Recently, some studies suggested that emission-based radiative forcing from BC has been reduced (Takemura and Suzuki, 2019; Lee et al., 2021) because

of carbon emission mitigation. However, the estimate is of a low confidence (Mcgraw et al., 2020). Aviation soot particles, directly emitted by commercial aircraft into the upper troposphere, exert net-warming effects on climate (Liou, 1986) by acting as potential ice-nucleating particles (INPs) at high altitudes where cirrus clouds usually form. Cziczo and Froyd (2014) suggested that aviation soot particles can engage in contrail evolution and cirrus formation by inducing ice crystal formation heterogeneously at aircraft cruise altitudes. McGraw et al. (2020) also suggested that the largest uncertainty of soot particle climate impacts lies in the cirrus cloud regime. However, numerous studies reported that fresh soot particles are poor INPs and require high relative humidity (RH) and low temperature (T) conditions to form ice crystals (Möhler et al., 2005a; Friedman et al., 2011; Kanji et al., 2011). In order to understand the climate impact of soot particles, it is essential to improve the knowledge about their ice nucleation activities in the atmosphere.

In the atmosphere, ice crystals can either be formed via homogeneous freezing of liquid droplets or induced by insoluble aerosol particles via heterogeneous ice nucleation (Vali et al., 2015). Homogeneous ice formation can only be triggered at $T < 235$ K (homogeneous nucleation temperature, HNT) and relative humidity with respect to ice (RH_i) higher than 140 % (Koop et al., 2000), where the nucleation rates of liquid aerosol particles are large enough to freeze spontaneously, leading to cirrus cloud formation. However, heterogeneous ice nucleation has a lower ice nucleation energy barrier with the aid of an INP which promotes the critical nucleation condition by providing an external surface for ice embryo formation. This is considered an important pathway for ice crystal formation at cirrus altitudes (Cziczo et al., 2013). In general, heterogeneous ice nucleation can occur at lower RH_i (< 140 %) conditions or warmer temperatures ($>$ HNT) with the presence of INPs in the atmosphere compared to homogeneous nucleation conditions. For example, Cziczo et al. (2013) reported that heterogeneous ice nucleation dominates the ice crystal formation process in cirrus clouds, depending on RH conditions as well as associated INP concentrations at cirrus altitudes. Before participating in an ice nucleation event, soot particles may interact with gaseous sulfur species in aircraft exhaust and can be coated by H_2SO_4 in the aviation plume (Chen et al., 1998). For instance, both sulfur oxides and water vapour are the products of aviation fuel combustion (Braun-Unkhoff et al., 2016), which can form supersaturated binary H_2SO_4–H_2O solutions (Curtius, 2002) in aviation plumes. Wyslouzil et al. (1994) treated single soot particles in a gaseous H_2SO_4 atmosphere to investigate their hydration behaviour and found mass increase in the soot particle by 14 ± 6 % due to addition of H_2SO_4, equivalent to 0.1 % of the SO_2 in the aircraft plume ending up as a H_2SO_4 coating on the soot particle surface. It is conceivable that soot particles and H_2SO_4 can be internally mixed and form H_2SO_4-coated soot particles in the atmosphere, especially in high-altitude aircraft corridors

where aeroengines emit fossil fuel combustion aerosol. In addition, some soot particles, generated by incomplete combustion from natural and anthropogenic sources contaminated by sulfur material during industrial processes, can get advected to the upper troposphere by vigorous convection (Pósfai et al., 1999; Okada et al., 2005; Motos et al., 2020). Therefore, both bare and H_2SO_4-coated soot particles should be considered in the study of cirrus cloud formation and corresponding climate impacts. The coating material modifies both chemical and physical properties of bare soot particles (Bond et al., 2013). The increased heterogeneity of coated soot particles is a significant source of uncertainty for evaluating their ice nucleation abilities. For instance, soluble sulfate material is suggested to increase soot particle water adsorption and may change its water interaction ability (Friedman et al., 2011). However, Kärcher and Lohmann (2002) reported that sulfate aerosol particles are unlikely to exert a sensible influence on cirrus cloud formation, with evidence suggesting internally mixed soot and sulfate particles may play a limited role in modifying background cirrus clouds in the atmosphere. Thus, the internal mixing of soot particles with H_2SO_4 may regulate its ability to be a potential INP, but the mixing state is unconstrained.

Ice nucleation of aviation soot particles and their surrogates has been investigated in both field measurements (Brown, 2018) and laboratory studies. The former shows that soot is present in contrail cirrus ice crystal residues, suggesting that soot particles can act as potential INPs for cirrus cloud formation upon contrail dissipation (Kärcher et al., 2018). In situ observations also provide some evidence that the number of soot particles emitted by per unit mass of fuel burnt increases with increasing distance downstream of the aviation plumes, whereas the ice crystal numbers in the contrail decrease by an equivalent fraction (Kleine et al., 2018), which suggests soot particles are initially embedded in contrail ice and then can be released into the upper troposphere after contrail dilution and sublimation (dissipation) processes. In addition, soot with a more compacted morphology than the freshly emitted particles is detected in aviation contrail ice crystal residues (Colbeck et al., 1990; Petzold and Schröder, 1998; Petzold et al., 1998), suggesting a change in the shape and size of the soot aggregates due to contrail processing.

Laboratory studies focus on the ice nucleation mechanism of aviation soot particle surrogates to understand which particle physiochemical property modulates their ice nucleation activities. Popovicheva (2004) suggested that hydrophobic soot particles, containing a few water-soluble materials, only initiate ice nucleation at $T <$ HNT by deposition nucleation. Möhler et al. (2005b) and Kanji et al. (2011) also reported that graphite soot particles can induce ice formation below homogeneous freezing conditions at $T < 238$ K. During deposition nucleation, it is assumed that there is no presence of a liquid phase, but the water vapour directly deposits onto the particle surface and nucleates ice crystals. Mahrt

et al. (2018) demonstrated that pore condensation and freezing (PCF) (Koehler et al., 2009; Marcolli, 2014) rather than deposition nucleation is responsible for soot particle ice nucleation activities, given that porous soot particles are able to form ice crystals at RH_i values lower than homogenous freezing conditions at $T <$ HNT. Previous studies also suggested that soot particle ice nucleation ability depends on its morphology and size (Mahrt et al., 2018; Nichman et al., 2019), hydrophilic and hydrophobic properties (Koehler et al., 2009; Biggs et al., 2017), chemical composition and surface chemical characteristics (Möhler et al., 2005a; Schill and Tolbert, 2012; Xue et al., 2019), surface oxidation levels (Whale et al., 2015; Hausler et al., 2018), as well as the particle water interaction history (Marcolli, 2017; Mahrt et al., 2020a, b). Most recently, Marcolli et al. (2021) suggested that the soot PCF process fundamentally requires optimum pore structure, size and appropriate surface wettability of the soot particle. Numerous factors involved in determining the ice nucleation activity of bare soot particles can render the impacts of the aging process on ice nucleation, where soot becomes internally mixed with other aerosols further changing the particle properties, more complicated. Therefore, systematic laboratory experiments to reveal the ice nucleation activity of certain soot samples and soot particles in different coating states are needed.

A foreign coating material changes the chemical composition and hygroscopicity of soot particles significantly (Zhang et al., 2008; China et al., 2015; C. Zhang et al., 2020). Zhang and Zhang (2005) showed that H_2SO_4 coating onto soot particles, produced by a soot generator burning methane, hexane or kerosene, is irreversible and enhances its hygroscopicity. Möhler et al. (2005b) reported that polydisperse graphite spark soot particles coated with H_2SO_4 nucleate ice at an ice saturation level higher than that of bare graphite spark soot particles but lower than the homogeneous freezing RH (RH_{hom}) required by pure H_2SO_4 droplets, at a given T. However, the soot coating thickness effect on ice nucleation was not systematically compared in the study because H_2SO_4-coated soot particles were produced with different coating conditions. Kulkarni et al. (2016) observed toluene- or α-pinene-coated diesel soot particles freezing homogeneously. Dalirian et al. (2018) investigated the coating effect of different organic compounds on the cloud droplet activation ability of soot particles and concluded that even a small amount of soluble coating is able to make hydrophobic soot particles become hydrophilic enough to be active cloud condensation nuclei (CCN). Therefore, the water interaction behaviour of coated soot particles can be changed significantly by the coating material. Considering its solubility in water and strong hygroscopic ability, H_2SO_4 coating very likely enhances soot particle surface wettability, i.e. a lower soot–water contact angle (Mahrt et al., 2020a), which plays an important role in PCF (David et al., 2020; Marcolli et al., 2021). In addition, the coating process can alter soot particle morphology and influence the availability of poten-

tial pores for PCF under cirrus cloud conditions. It is reported that external material coating changes the initial soot particle size, particle internal microstructure and surface texture (Saathoff et al., 2003; Khalizov et al., 2009; Pei et al., 2018; C. Zhang et al., 2020). The size growth caused by considerable addition of coating material is a possible coating effect, and the coating material distribution may further modify the soot-aggregate structure. For example, oleic acid coating can significantly deform soot particle shape and increase particle mass, whereas the removal of the coating material by heating seems to recover its morphology to some extent (Bambha et al., 2013). Schnitzler et al. (2017) also demonstrated that liquid material coating can change soot-aggregate structure by the tension induced by coating condensation on the particle surfaces. It is therefore possible that, if the particle structure can be changed, the pore volume and pore size distribution of the soot aggregate are also alterable. Considering that soot particle ice nucleation ability via PCF shows dependence on the aforementioned parameters, coating effects on soot particle ice nucleation could benefit from systematic studies with a focus on associated morphology and hygroscopicity changes.

In this study, both a propane (C_3H_8) combustion soot and a porous commercial carbon black are exposed to different H_2SO_4 supersaturation levels to generate coated soot particles. With progressively increasing H_2SO_4 coatings, size-selected soot particle ice nucleation activities are systematically investigated in the mixed-phase and cirrus cloud regimes and compared to bare soot particles. The mixing state of a soot particle with H_2SO_4 is characterized with an emphasis on the morphology, and a hypothesis about the coating process of a soot particle with H_2SO_4 and the influence on cirrus ice nucleation is proposed based on the results presented herein.

2 Experimental methods

2.1 Soot samples

In this study, two types of soot particles were investigated. First, a C_3H_8 flame soot is produced by a miniature combustion aerosol standard (miniCAST, model 4200, Jing Ltd., Zollikofen, Switzerland) soot generator. The Jing miniCAST forms a diffusion flame by burning C_3H_8 under fuel-lean conditions. The associated soot particle is termed mCAST-black hereafter. This soot sample is technically the same as the sample used by Mahrt et al. (2018, 2020a, b), who studied the ice nucleation activities of fresh and aged mCAST-black soot particles in the continuous-flow diffusion chamber – the horizontal ice nucleation chamber (HINC) (Lacher et al., 2017). At the outlet of the miniCAST, part of the exhaust, containing primary soot particles or small-sized aggregates, is diluted by filtered synthetic air. The resulting flow containing aerosol is then fed into a 0.125 m^3 continuous stirred tank reactor to generate larger and more homogeneous soot aggre-

gates. Finally, a 1 L min^{-1} sample flow is sampled out of the tank and directed to a differential mobility analyser (DMA, classifier 3080, with a 3081 column and a polonium radiation source, TSI Inc.) after passing through a molecular sieve diffusion drier, in order to select a monodisperse aerosol sample with a mobility diameter of 200 or 400 nm at RH$_w$ < 5 %.

The second type of soot is FW200, a commercial carbon black (Orion Engineered Carbons GmbH, OEC, Frankfurt am Main, Germany). FW200 carbon black is a product of incomplete combustion from hydrocarbon liquid fuels. There are two purposes here for choosing this commercial carbon black as one of the experimental samples. Firstly, it is used to represent porous and surface wettable soot particles in the atmosphere because of its large specific surface area value (550 m^2 g^{-1} provided by the manufacturer; 526 m^2 g^{-1} reported by Mahrt et al., 2018) and according to surface chemistry information provided by the manufacturer. Secondly, future studies can reproduce ice nucleation experiments with this commercial carbon black more precisely for analysis and comparisons. Mahrt et al. (2020a) used a wet dispersion method to aerosolize soot particles aged in H$_2$SO$_4$ (pH = 4) by a nebulizer with a magnetic stirrer. Instead of using an aqueous suspension, a dry dispersion method is utilized in this study to reduce changes in morphology caused by droplet evaporation after wet suspension. A Venturi nozzle is deployed with a glass jar containing dry soot powder mounted on a strong magnetic stirrer. Soot powder is suspended by the stirrer and then can be entrained into a high-pressure N$_2$ flow by the nozzle. The soot aerosol flow generated is directed to a flow cascade to buffer the aerosol flow and particle number concentration fluctuations. Finally, a 1 L min^{-1} sample flow is directed to the DMA, and 200 or 400 nm size-selected soot particles can be generated.

2.2 Instrumentation

Figure 1 shows the experimental set-up schematic illustrating aerosol sample generation, sample particle size selection, soot particle H$_2$SO$_4$ coating, ice nucleation experiments and particle characterization measurements. Firstly, the DMA selects soot particles with a mobility diameter of 200 nm (sheath to sample flow ratio 13 : 1) or 400 nm (sheath to sample flow ratio 7 : 1), and a 1 L min^{-1} monodisperse sample flow is produced with a particle number concentration larger than 3000 cm^{-3} for the following experiments. The aerosol sample (1 L min^{-1}) either goes through an in-house-built H$_2$SO$_4$-coating apparatus or passes by a dilution system with synthetic airflow. This dilution system has equivalent volume and flow resistance to the coating apparatus as well as the same dilution ratio ($\sim$ 5 : 1). The diluted or H$_2$SO$_4$-coated soot aerosol sample (> 5 L min^{-1}) is split into five pathways, distributed to a high-efficiency particulate air capsule (HEPA capsule, PALL Corporation) for exhaust flow, a condensation particle counter (CPC; Model 3772, TSI Inc.) for particle number concentration counting (1 L min^{-1}), an

ice nucleation experiment flow (0.22 L min^{-1}) to the HINC (Lacher et al., 2017), a scanning mobility particle sizer (SMPS, Classifier 3082, Column 3081, CPC 3776 low-flow mode 0.3 L min^{-1} or CPC 3772 1 L min^{-1}, TSI Inc.) flow for particle size distribution measurement, a centrifugal particle mass analyser (CPMA, Cambustion Ltd., Cambridge, UK) flow (1.5 L min^{-1}) pulled by a CPC (Model 3787, TSI Inc.) for particle mass distribution measurement, and a sample flow (1 L min^{-1}) for microscopy grids collection by the Zurich Electron Microscope Impactor (ZEMI) (Mahrt et al., 2018). The purpose of this study is to generate H$_2$SO$_4$-coated size-selected soot particles and to study their properties for mobility diameter, mass (density), morphology and ice nucleation ability.

2.2.1 Coating apparatus

The coating procedure follows the basic idea of heating to produce coating material vapour and then cooling to condense or adsorb the coating material onto soot particle surfaces, consequently generating H$_2$SO$_4$-coated soot particles, as depicted in Fig. 2. The coating mechanism is attributed to two pathways, including the direct condensation of supersaturated H$_2$SO$_4$ vapour and the adsorption of small H$_2$SO$_4$ particles formed by homogeneous nucleation (Bambha et al., 2013; Pei et al., 2018). The aerosol sample flow used to generate H$_2$SO$_4$ vapour is heated in an aluminium heating block before going through a flask containing 50 mL pure H$_2$SO$_4$ (Sigma-Aldrich, 95.0 %–97.0 %) mounted on another aluminium heating block. The temperature of the heating blocks is controlled by a LabVIEW (National Instruments Corporation, Austin, Texas, US) program. While passing through the H$_2$SO$_4$ flask, soot particles will be mixed with H$_2$SO$_4$ vapour. Next, a dilution flow at the same temperature as the H$_2$SO$_4$ / soot flow entrains the particles out of the flask. Downstream of the apparatus, there is a water-cooling system to generate H$_2$SO$_4$ supersaturation to nucleate or condense H$_2$SO$_4$ onto soot particle surfaces, thus generating H$_2$SO$_4$ internally mixed soot particles. The cooling water temperature is maintained at 20 °C by a thermostat (LAUDA E300). By increasing the H$_2$SO$_4$ saturation and dilution flow temperature from 30 to 95 °C, the H$_2$SO$_4$ coating wt % (refer to Sect. 2.2.3, Eq. 1) in terms of the ratio of H$_2$SO$_4$ coating mass to the bare soot particle mass can be increased monotonically.

In order to generate internally mixed soot / H$_2$SO$_4$, the following operational procedure is strictly followed. First, a particle-free synthetic airflow is used to flush the apparatus for several minutes at the very beginning of the experiment until the CPC records a zero particle number concentration at the outlet of the coating apparatus. Then, the heated soot aerosol sample flow is connected to the inlet of the apparatus. In order to check the particle mixing state, a SMPS–CPMA combined particle size and mass distribution measurement is conducted at the outlet of the coating apparatus before
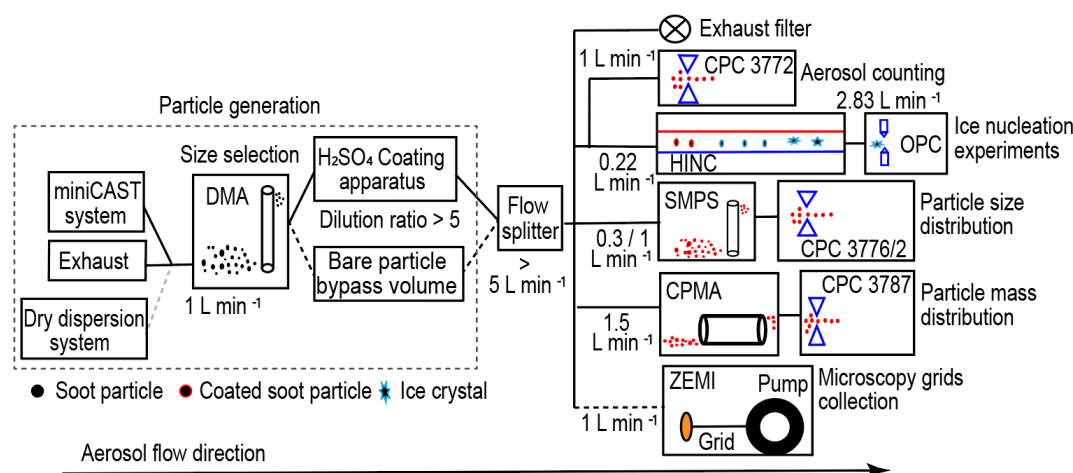
Figure 1. Schematic of the experimental set-up. miniCAST: miniature Combustion Aerosol Standard; DMA: differential mobility analyser; CPC: condensation particle counter; HINC: horizontal ice nucleation chamber; OPC: optical particle counter; SMPS: scanning mobility particle sizer; CPMA: centrifugal particle mass analyser; ZEMI: Zurich Electron Microscope Impactor.
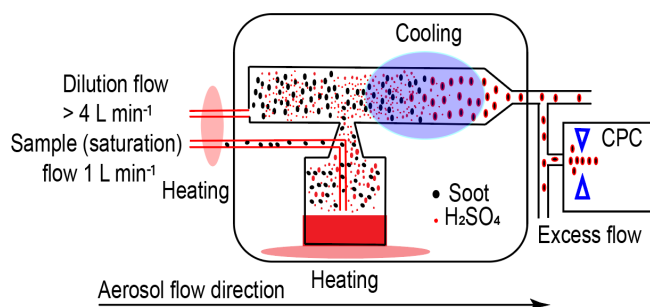

Figure 2. The schematic of the coating apparatus. Red line denotes heated tubing. Light red-shaded area denotes the heating block. Purple-shaded area denotes the water cooling system.

starting the downstream experiments. The results demonstrate that only internally mixed soot particles with H_2SO_4 are produced from the coating apparatus, indicating no pure nucleated H_2SO_4 (see Appendix A and the discussion below). The SMPS results for the 200 nm mCASTblack soot particle coating process are presented in Appendix Fig. A1 as an example. In the absence of soot, nucleation-mode H_2SO_4 shows a high number concentration and a small-sized mode of ~ 40 nm fitted by a log-normal distribution function. After feeding soot samples into the coating apparatus, mixed aerosol particle size distribution mode shifts close to the size mode of bare soot particles; meanwhile, the small-sized mode of H_2SO_4 particles is absent and the number concentration of H_2SO_4 particles reduces to effectively zero for the ~ 40 nm peak (see Fig. A1). The CPMA mass scan results also show the homogeneity of the 200 nm mCASTblack soot particles internally mixed with H_2SO_4, given that the log-normal mass distribution fitting for coated aerosol particles only shows a single distinct peak (see Fig. A2), which in-

dicates the mass mode of the aerosol is for H_2SO_4-coated particles only. Considering that a 200 nm pure H_2SO_4 particle has a larger mass than a coated soot particle, we conclude that there is no pure 200 nm H_2SO_4 particle existing in the aerosol flow.

2.2.2 Ice nucleation experiments

In this study, the HINC chamber (Kanji and Abbatt, 2009; Lacher et al., 2017) is utilized to investigate particle ice nucleation abilities under varying RH conditions at a fixed temperature. HINC is a horizontal continuous-flow diffusion chamber in which aerosol particles can experience a defined RH and T condition for a variable time (~ 16 s in this study). Two parallel copper plates, sandwiching a polyvinylidene fluoride (PVDF; Angst + Pfister AG, Zurich, Switzerland) frame with a thickness of 20 mm, form the core chamber space. The temperature of each copper plate is controlled by a thermostat (LAUDA, RP890) and monitored by four thermocouples with an uncertainty of ± 0.1 K. Glass fibre paper (Pall Corporation, 66217) adhering to the inner wall of each copper plate is wetted before the experiment and serves as a water vapour reservoir. During the experiment, both walls are coated with a thin ice layer and remain at ice saturation condition ($RH_i = 100\%$). By maintaining a temperature difference (ΔT) between the top and bottom walls ($T_{top} > T_{bottom}$), a linear temperature distribution as well as a linear distribution of water vapour pressure develop inside the chamber in the vertical dimension. However, the saturation water vapour pressure has an exponential relation to the temperature. Hence, a non-linear RH distribution will be generated and the RH value at a fixed vertical position inside the chamber can be determined as well. Upstream of the chamber, there are four ports drawing pure dry N_2 into the chamber as the sheath flow confining the aerosol sample flow to

the centre of the chamber at a defined RH and T condition. A movable aerosol injector is used to direct the aerosol particles into the centre of the chamber and can also be used to adjust particle residence time in the chamber. At the chamber outlet, an optical particle counter (OPC, MetOne, GT-526S) maintains a total flow rate of 2.83 L min^{-1}. Before the HINC experiment, the N$_2$ sheath flow rate is adjusted to ensure that 0.22 L min^{-1} aerosol sample flow makes up part of the 2.83 L min^{-1}. A 1 : 12 aerosol sample to sheath flow ratio is used during the whole course of the study. During the HINC experiment, the CPC is used to count the total aerosol particle number entering the chamber and the OPC is used to detect the total number of ice crystals or water droplets coming out of the chamber in six size channels (0.3, 1.0, 2.0, 3.0, 4.0 and 5.0 μm). Thus, the ratio of ice crystal or water droplet number to the total aerosol particle number can be derived, which is the aerosol particle activated fraction (AF) value.

For bare and coated soot samples, HINC experiments are performed from 218 to 243 K with six measurements at different T and with a 5 K interval. At each T, at least two RH scans are conducted for each soot sample from ice saturation conditions to RH conditions above water saturation. The RH$_i$ scan rate is 2 % min^{-1}. The RH$_w$ values of the aerosol sample upstream of HINC are less than 5 % and monitored by a RH sensor. Soot particle H$_2$SO$_4$ coating wt % for ice nucleation experiments is shown in Table 1.

2.2.3 Particle characterization measurements

SMPS–CPMA. The aerosol particle size distribution is measured by a SMPS system after size selection and/or the coating process (see Fig. 1). For 200 nm size-selected soot particles with/without coating, the CPC 3772 with a flow rate of 1 L min^{-1} is used so that the SMPS measurement can cover a size scanning range from 12.6 to 572.5 nm, which means the double-charged particles selected by the DMA upstream can be detected. For 400 nm soot aerosol samples, the SMPS utilizes a low-flow mode CPC 3776 with a 0.3 L min^{-1} flow rate and can scan up to a size value of 914 nm, which also covers the 680 nm particles carrying two charges but is treated as a 400 nm particle by the upstream DMA. The number of double-charged particles is approximately 16 % and 29 % for 200 and 400 nm mCASTblack bare soot particles, respectively (see Fig. A3), and double-charged 200 and 400 nm FW200 bare soot particles amount to 21 % and 26 %, respectively (see Fig. A4). The CPMA is operated in mass scanning mode at a constant speed. A water CPC 3787 running in high-flow mode (1.5 L min^{-1}) is used to sample the aerosol through the instrument. The mass scanning range covers the mass value of double-charged particles (see Fig. A2). Single particle mobility diameter is derived from a log-normal fitting of the aerosol size distribution measured by SMPS, assuming soot particles to be spherical. The mass value of a single particle is derived from CPMA mass distribution scans with a similar data processing method. Based on sin-

gle soot particle mobility diameter and mass results, H$_2$SO$_4$ coating wt %, equivalent coating monolayers (assuming uniform coating) and particle effective density are calculated. The H$_2$SO$_4$ coating wt % is the ratio of soot-particle-coated H$_2$SO$_4$ mass to the mass of the initial bare soot particle and is defined as

$$wt = \frac{x - y}{y} \times 100, \tag{1}$$

where x is the mass of the H$_2$SO$_4$-coated soot particle and y is the bare soot particle mass. The number of equivalent coating monolayers (MLs) is calculated according to Wyslouzil et al. (1994) and given by

$$ML = \frac{wt \cdot N_A}{100 M_W \cdot S \cdot N_M}, \tag{2}$$

where wt is the coating mass percentage value, N_A is the Avogadro constant, M_W is the molecular weight of H$_2$SO$_4$, N_M is the number of H$_2$SO$_4$ molec. cm^{-2} corresponding to one monolayer coverage (4.5×10^{14} cm^{-2}) (Wyslouzil et al., 1994), and S is the specific area of the soot particle (mCAST-black 120 m^2 g^{-1}, FW200 526 m^2 g^{-1}) (Mahrt et al., 2018). According to McMurry et al. (2002), the particle effective density (ρ_{eff}) expression is given as

$$\rho_{eff} = \frac{6m}{\pi \cdot d^3}, \tag{3}$$

where m is the single particle mass and d is the particle mobility diameter. To control the H$_2$SO$_4$ coating wt %, a number of factors need to be considered, including initial soot aerosol particle number concentration, saturation and dilution flow rate and temperatures, the temperature of pure H$_2$SO$_4$ in the flask and subsequent cooling condition (see Fig. 2), the set-up volume, as well as the intrinsic soot particle properties. Here, temperatures, flow rates and the whole volume of the apparatus are well controlled. However, it is impossible to adjust the initial soot sample particle number concentration to be identical for every experiment. As a result, even though the H$_2$SO$_4$ coating thickness increases with increasing H$_2$SO$_4$ saturation temperatures, for per soot sample coating, the result shows some variance. In this study, the standard deviation value for each coating wt % is provided in Table 1 and in each panel of Fig. 3.

The H$_2$SO$_4$ coating wt %, particle mobility diameter, particle ρ_{eff} and equivalent ML value for each soot sample are presented in Fig. 3. Note that the equivalent ML values highly depend on the soot-particle specific surface area given by BET (Brunauer–Emmett–Teller) analysis (Brunauer et al., 1938), which can be influenced by different pre-treatment levels and also different gas probes used in the physisorption measurement (Lowell et al., 2004). For example, Ouf et al. (2019) reported that soot BET specific surface area can be severely influenced by the sample outgassing level and can vary in a significant range. Furthermore, it is suggested

Table 1. The ratio of coated H_2SO_4 mass to the bare soot particle mass (wt %) for 200 and 400 nm mCASTblack and FW200 soot particles. The uncertainty represents 1 standard deviation.

H_2SO_4 evaporation T (°C)	H_2SO_4 coating wt %			
	mCASTblack		FW200	
	200 nm	400 nm	200 nm	400 nm
30	2.7 ± 1.9	$1.9 \pm 3.5*$	3.5 ± 2.6	$1.8 \pm 2.3*$
35	5.4 ± 2.0	4.2 ± 3.9		3.8 ± 1.5
40	8.5 ± 3.6	6.2 ± 4.3	9.3 ± 2.8	6.1 ± 1.8
45	10.9 ± 2.9		15.0 ± 4.1	8.0 ± 2.0
50	15.6 ± 2.4	10.9 ± 4.4	18.1 ± 3.8	8.7 ± 1.4
55	19.5 ± 3.1	13.7 ± 3.7	22.3 ± 3.7	
65	24.2 ± 3.8	20.9 ± 3.5	28.8 ± 4.8	10.8 ± 2.6
75		23.6 ± 4.2		18.8 ± 2.7
80	28.1 ± 4.8		40.3 ± 4.5	
85		$31.1 \pm 4.6*$		26.4 ± 2.9
95			135.3 ± 7.6	$65.0 \pm 4.2*$

* Denotes samples that are analysed with the SEM technique (see Sect. 3.3.1).

that N_2 BET and argon BET results for the same soot sample show variance (Lowell et al., 2004). Nevertheless, the results in Fig. 3 can still provide relatively comparable information to evaluate soot particle mixing states with different H_2SO_4 coating thicknesses. Overall, the 200 nm size-selected soot particle mobility diameter can mostly increase by ~ 5 % with increasing H_2SO_4 coating wt % but start to decrease dramatically when the H_2SO_4 coating wt % is larger than ~ 20 %, which means first size growth and then shrinkage (collapse). However, such a small-sized growth is absent for the case of 400 nm soot particles, and the size starts to decrease due to collapse when the coating mass percentage reaches ~ 20 %. This may result from a lower effective density of the 400 nm soot particle compared to that of the 200 nm soot particle, which suggests larger soot particles are less densified and contain more pore volume for H_2SO_4 filling rather than surface accumulation of the acid, which would lead to a detectable size increase. With increasing coating wt %, the equivalent H_2SO_4 coverage ML and coated particle ρ_{eff} increase monotonically, as expected.

Scanning electron microscopy (SEM) (Zeiss Leo 1530, Carl Zeiss AG, Oberkochen, Germany) is used to observe the H_2SO_4 coating state on soot particles. Both coated and uncoated FW200 and mCASTblack 400 nm soot aggregates are collected on 400 mesh Cu girds with a formvar/carbon support film (TED, PELLA, Inc.). All grids are collected using ZEMI, an in-house-built and semi-automated rotating drum impactor (Mahrt et al., 2018) running in parallel to HINC ice nucleation experiments. During the grid sampling, ZEMI pulls a $1 \, L \, min^{-1}$ aerosol sample flow as shown in Fig. 1. The total sampling time is between 5 and 10 min depending on the particle concentration. In addition to bare particles,

coated soot aggregates with the lowest and highest H_2SO_4 coating wt % (see Table 1) in the ice nucleation experiments are collected for SEM analysis. For convenience of discussion in Sect. 3, these two coated conditions will be termed thin coating and thick coating, respectively. Images of interest are obtained at magnification values 20 and 200 k. The small magnification value is used to have an overview of the particles. Soot particle morphology change and H_2SO_4 coating state are analysed from high-resolution images.

Transmission electron microscopy (TEM) and high-resolution TEM (HR-TEM) (JEOL-1400+ TEM, JEOL Ltd., Tokyo, Japan, operated at 120 kV; Hitachi HT7700 EXALENS, Hitachi Ltc., Chiyoda, Japan, operated at 100 kV; TFS Talos F200X, operated at 200 kV, and TFS F30, operated at 300 kV, both Thermo Fisher Scientific Inc., Waltham, MA, USA) are utilized to detect morphology changes induced by H_2SO_4 coating and physical evidence of H_2SO_4 coating. These grids were collected separately from the SEM grids. To match with corresponding ice nucleation experiments, the coating wt % (see Table 2) of soot aggregates for TEM analysis was controlled to be comparable to those coating wt % shown in Table 1 for 200 nm soot samples. Again, the lower H_2SO_4 coating wt % will be termed thin coating and the higher one will be termed thick coating for further SEM result discussion. Both bare and coated soot aggregates are collected on Quantifoil Cu 200 mesh R2/2 grids (Quantifoil Micro Tools GmbH, Großlöbichau, Germany). Open holes of the R2/2 pattern provide a view of soot aggregates without a carbon film background.

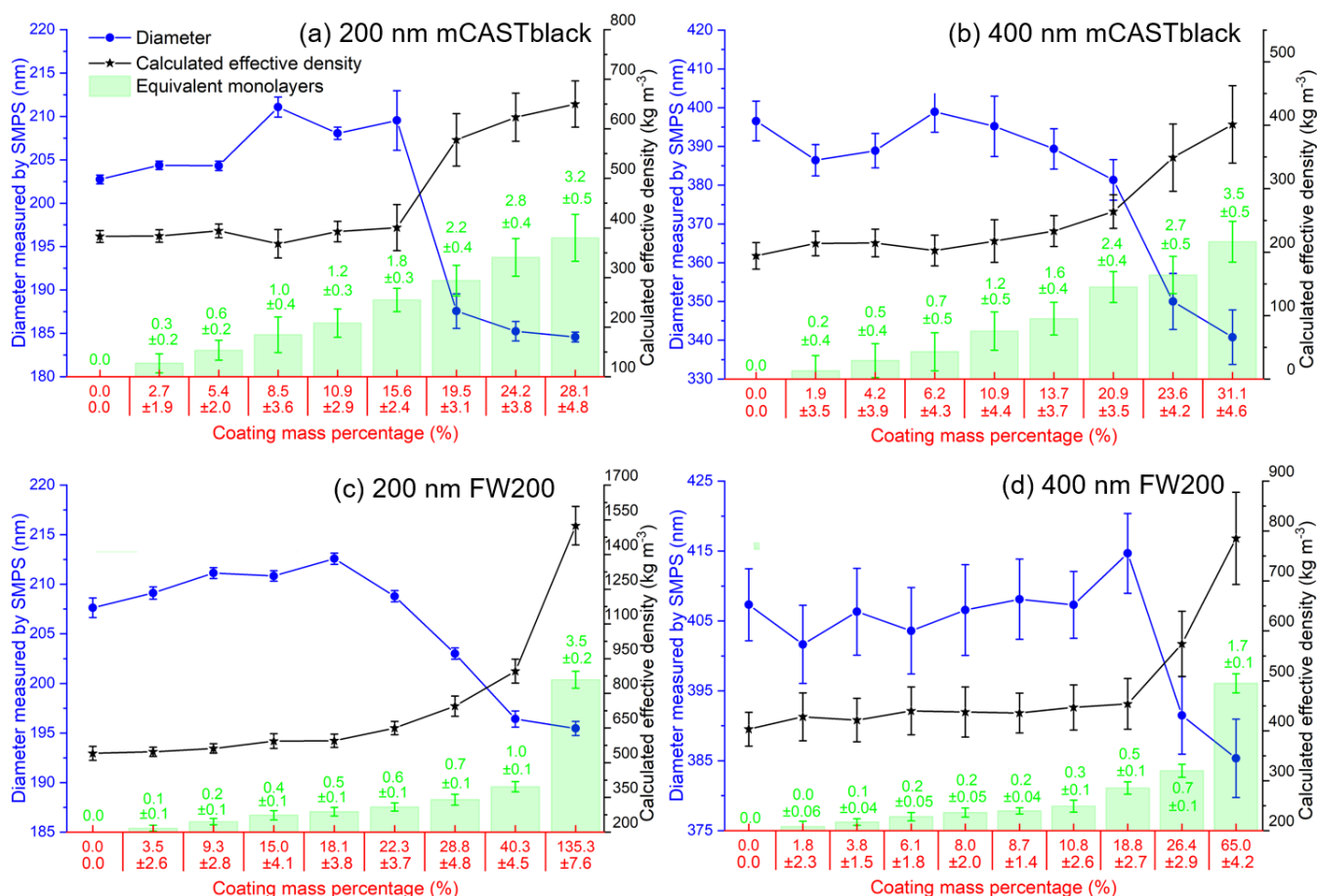Energy-dispersive X-ray spectroscopy (EDX) (TFS Talos F200X equipped with a Super-X EDS system) is used for

Figure 3. The mobility diameter, calculated effective density and the number of equivalent H_2SO_4 coating monolayers of mCASTblack 200 **(a)** and 400 nm **(b)** and FW200 200 **(c)** and 400 nm **(d)**.

Table 2. The ratio of coated H_2SO_4 mass to the bare soot particle mass (wt %) for 200 nm mCASTblack and FW200 soot aggregates collected for TEM analysis. The uncertainty represents 1 standard deviation.

H_2SO_4 evaporation T (°C)	H_2SO_4 coating wt %	
	mCASTblack (200 nm)	FW200 (200 nm)
30	2.9 ± 2.8	2.3 ± 2.2
80	30.2 ± 3.3	
95		139.3 ± 10.8

chemical evidence of the presence of H_2SO_4 on soot particle surfaces. These grids used for EDX are the same as those for the TEM measurements. Both bare and coated soot aggregates are analysed, and results are presented by both 2D element distribution maps and conventional element spectra. Carbon (C), oxygen (O) and sulfur (S) element mass contents for soot particles with different H_2SO_4 coating wt % are also calculated and normalized to compare their chemical composition change.

3 Results and discussion

Soot particle ice nucleation abilities are presented in terms of AF curves as a function of RH_w and RH_i in Figs. 4 to 7. The 1 μm OPC channel data are used to plot AF curves, referring to the ratio of the total number of particles exiting the HINC chamber larger than 1 μm to the total number of particles entering the chamber as sampled by the CPC. The particle property results obtained by characterization measurements in Sect. 2 will be used to understand the corresponding soot particle ice nucleation activities. Figures 4 and

5 present the AF plots for coated 200 and 400 nm mCAST-black particles and uncoated counterparts as a function of RH values at T from 218 to 243 K. Ice nucleation activities of bare and coated 200 and 400 nm FW200 particles are shown in Figs. 6 and 7, respectively. Both bare mCASTblack and FW200 soot particles can only form water droplets above water saturation conditions at 243 and 238 K ($T >$ HNT), regardless of particle size. At these two temperatures, OPC signals are only observed at small channels, but signals are absent at the largest channel, i.e. the 5 μm channel (see Figs. B5 to B8). This is because water droplet growth by vapour diffusion is less efficient than that of ice crystal growth under these conditions ($RH_w < 105$ %) in HINC (Lohmann et al., 2016). Thus, water droplets do not grow up to 5 μm and are thus not detected in the 5 μm OPC channel; however, ice crystals can grow up to this size value (Lacher et al., 2017; Mahrt et al., 2018). Therefore, we conclude no ice nucleation onto bare soot particles at 243 and 238 K. This is in agreement with Kanji et al. (2020), who suggested that commercial black carbon particles require temperatures lower than HNT to freeze. For mCASTblack, ice nucleation results were the same for both 200 and 400 nm particles, showing no significant activation at $RH < RH_{hom}$ at cirrus-relevant temperatures ($T <$ HNT). FW200 particles exhibit significant ice nucleation at $T <$ HNT, unlike mCASTblack, with 400 nm FW200 particles being more active INPs than 200 nm samples. Unsurprisingly, excellent agreement is achieved for the results of bare mCASTblack and FW200 soot between this study and Mahrt et al. (2018), who also studied these two types of soot INP samples using the same chamber. At $T <$ HNT, AF curves for bare mCASTblack soot particles stay in the uncertainty range of homogeneous freezing. As shown in Figs. 4 and 5, only $< 10^{-3}$ of the soot sample can form ice crystals at RH values slightly lower than the homogeneous RH values, even at 218 K. This is consistent with the results from Mahrt et al. (2018, 2020a, b). As shown in Figs. 6 and 7, bare FW200 soot particles are active INPs and can form ice crystals at $RH < RH_{hom}$ when $T <$ HNT, also in line with the results presented by Mahrt et al. (2018). The authors suggested that these soot particles with small mesopores can be effective INPs and form ice crystals via PCF at humidity conditions lower than homogeneous freezing conditions in the cirrus cloud regime (Mahrt et al., 2018). Herein, mesopores are defined as pore structures with a width between 2 and 50 nm, whereas pore structures with a width less than 2 nm refer to micropores (Thommes et al., 2015). The paucity of mesopores relevant to PCF and its low surface wettability make mCASTblack soot a poor INP at $T <$ HNT compared to FW200 soot. Here, PCF-relevant mesopores refer to pores with the right size and shape which are not only small enough to induce liquid water capillary condensation at $RH_w < 100$ % due to the inverse Kelvin effect, but also large enough to allow ice growing out of the pore upon homogeneous freezing of supercooled porewater (Marcolli, 2014, 2020). The active ice nucleation ability of FW200 can be attributed to its low soot–water contact angle and abundant mesopore structures.

In addition to bare soot particles, more than eight different H_2SO_4 coating wt % are performed from less than one equivalent molecule monolayer to several equivalent molecule monolayers' coverage. For ease of discussing the ice nucleation activity comparison between bare and coated particles, three typical coating states, namely thin, medium and thick coating, are selected as representative cases. The results for all coating wt % corresponding to Table 1 are given in Appendix B, Figs. B1 to B4. Thin coating stands for a H_2SO_4 coating wt % of less than 3.5 % of its initial mass value. Medium coating represents a H_2SO_4 coating of wt % ~ 10 %, whereas thick coating represents a H_2SO_4 coating of wt % larger than 25 %.

3.1 H_2SO_4-coated mCASTblack soot ice nucleation results

At $T >$ HNT (243 and 238 K), both coated and uncoated particles require water saturation conditions to form water droplets. With similar evidence of bare particles, we conclude no ice nucleation at $T >$ HNT for coated soot of all coating masses. Soot particles coated with H_2SO_4 are expected to be more hygroscopic and act as CCN if a uniform coating is assumed. However, the AF curves for both 200 and 400 nm coated mCASTblack soot stay within error bars with those of bare particles at $T >$ HNT, as shown in Figs. 4 and 5. There is some indication that coated particles are better CCN at $T >$ HNT. However, we cannot claim that the hygroscopicity is significantly different than seen in the AF curves overlapping with those of bare soot particles, suggesting that the coatings may be non-uniform but form clusters on soot aggregates. Non-uniform coating patterns can be seen from SEM images in Fig. 8. Muller et al. (1996) and Persiantseva et al. (2004) suggested that soot particle micropores (< 2 nm) play an important role in the soot–water interaction activities if there is no soluble material available on its surfaces. Popovicheva et al. (2008a, b) demonstrated that capillary condensation induced by mesopores in soot aggregates can occur when RH_w values are larger than 80 %. Therefore, it is feasible that a small amount of H_2SO_4 coating on a mCASTblack particle impacts its soot–water interaction activities if non-uniformly distributed coating material leads to pore filling, which reduces mesopore availability. However, if further H_2SO_4 coating provides soluble material on soot surfaces for water adsorption, it compensates for the unavailability of pores caused by thin coating pore filling and enhances soot uptake ability because of its high hygroscopicity. Overall, there is no significant change for mCASTblack soot CCN activity after H_2SO_4 coating using the method presented in this work.

At $T <$ HNT (233–218 K), all coated particles only form ice via homogeneous freezing, and there is an apparent freezing depression, particularly at 223 and 218 K for thinly
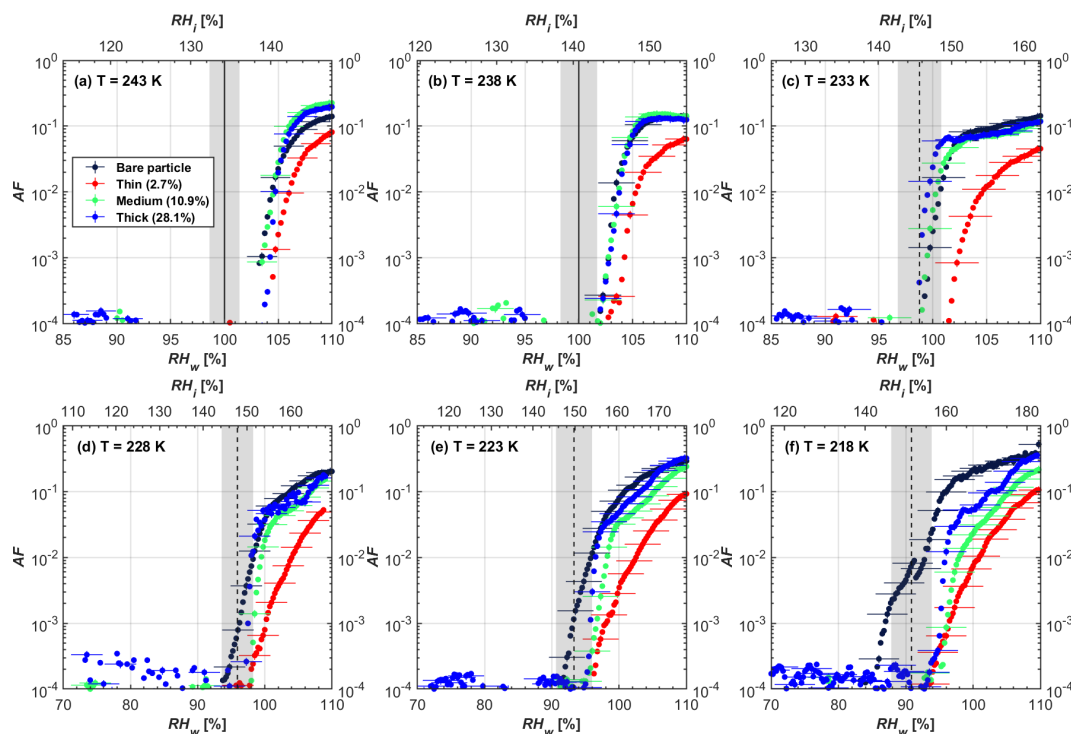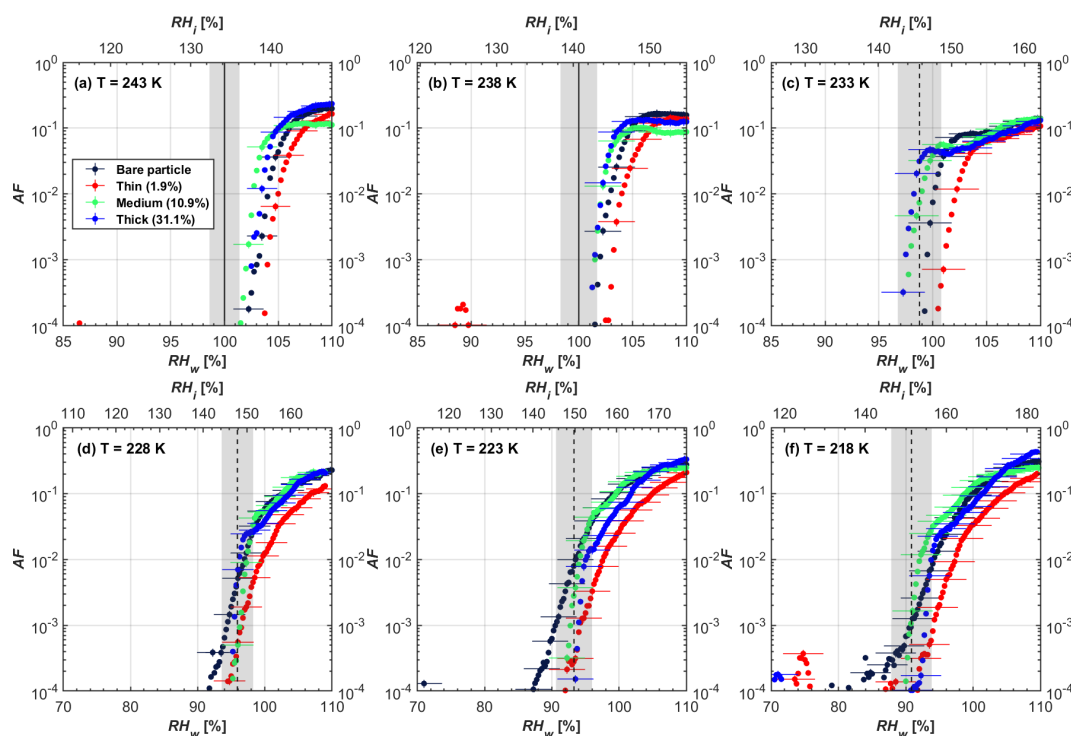
Figure 4. AF as a function of RH at the given temperatures for 200 nm mCASTblack soot particles. Black solid lines represent water saturation conditions according to Murphy and Koop (2005). Black dashed lines denote the expected RH values for solution droplet homogeneous freezing at $T <$ HNT (Koop et al., 2000). The grey-shaded area shows the possible RH variation and uncertainty in HINC for the calculated water saturation and homogeneous freezing conditions. The percentages represent the H_2SO_4 coating wt %.

coated soot, as can be seen in Figs. 4 and 5 by the delayed freezing onset of coated particles compared to that of bare particles at each T. This implies that H_2SO_4 coating inhibits the PCF mechanism at these low T. In Fig. 4, thinly coated 200 nm mCASTblack soot particles show the largest suppression in the onset of ice formation among all coating masses. This is coherent with the results at warm temperatures ($T >$ HNT) and can be explained by the H_2SO_4 pore-filling effect. Homogeneous freezing of supercooled water in pores is an important step in a PCF activation process (Marcolli et al., 2021; Marcolli, 2014). According to Koop et al. (2000), the homogeneous freezing rate depends on the liquid water activity. Due to H_2SO_4 filled in pores for thin coating cases, inverse Kelvin effect induced water uptake will form a high-concentration H_2SO_4 solution with a low water activity, which leads to depressed homogeneous freezing as it requires higher RH_w conditions than RH_{hom} for freezing. This inhibits the bulk freezing of the soot particle with low H_2SO_4 coating wt % until the particle takes up sufficient water to dilute enough for bulk droplet freezing. With more coating (in medium and thick cases), hygroscopic H_2SO_4 adsorption on soot surfaces may occur simultaneously with H_2SO_4 pore filling and thus enhance soot surface hygroscopicity. Hence, soot particles with medium or thick coating will not only sustain pore filling, but also form bulk water droplets

more readily. This can explain why the soot particle with thicker coating tends to freeze homogeneously like a bulk solution droplet under higher RH conditions. More details about the interaction of soot particles with H_2SO_4 will be discussed in Sect. 3.3. The similar ice nucleation activity of 400 nm coated mCASTblack soot particles can be seen from Fig. 5.

Results for coated mCASTblack soot in this study are comparable to the literature. For instance, ice nucleation results at low T are in good agreement with previous H_2SO_4-coated miniCAST C_3H_8 soot results from Crawford et al. (2011), who treated polydisperse miniCAST soot aerosol in saturated H_2SO_4 vapour and studied its ice nucleation behaviour at T from 220 to 230 K. Similarly, the authors concluded that the addition of H_2SO_4 inhibits soot particle ice activation and shifts the freezing onset RH towards the homogeneous freezing conditions of pure H_2SO_4. Möhler et al. (2005b) also reported a suppression in the ice nucleation ability of polydisperse graphite spark-generated soot samples (~ 25–300 nm) coated with H_2SO_4 (~ 40–350 nm) which freeze towards homogeneous freezing conditions. However, Mahrt et al. (2020a) reported a significant ice nucleation enhancement for 400 nm mCASTblack soot particles aged in a bulk H_2SO_4 aqueous solution (pH $= 4$) and coated by dry residues of H_2SO_4. The authors used a different aging

Figure 5. AF as a function of RH at the given temperatures for 400 nm mCASTblack soot particles. Black solid lines represent water saturation conditions according to Murphy and Koop (2005). Black dashed lines denote the expected RH values for solution droplet homogeneous freezing at $T <$ HNT (Koop et al., 2000). The grey-shaded area shows the possible RH variation and uncertainty in HINC for the calculated water saturation and homogeneous freezing conditions. The percentages represent the H_2SO_4 coating wt %.

method to treat the soot sample, and the H_2SO_4 aging effect and coating material distribution are different from the coating conditions in this study. The 400 nm particles in Mahrt et al. (2020a) were generated by atomizing a bulk aqueous suspension followed by drying and size selection. If a solution droplet spanning a size range from 400 nm to 2 μm is assumed before drying, the H_2SO_4 coating wt % is estimated to be in the range from 0.0026 % to 0.32 %, much less than the coating wt % in this study. Furthermore, the H_2SO_4 coating generated in this way can be distributed more uniformly over the soot particle surface compared to a non-uniform H_2SO_4 coating in this study (see Sect. 3.3). On the other hand, soot particles experienced a water interaction process when they were treated with H_2SO_4 aqueous solution, which means water interaction-induced morphology changes and particle compaction could be responsible for this ice nucleation promotion as suggested by the soot pure water aging case in the same study by Mahrt et al. (2020a). In addition, DeMott et al. (1999) investigated the freezing RH conditions for multiple-layer H_2SO_4-coated polydisperse lamp black soot particles (Degussa Corporation, Frankfurt, Germany) with a size distribution mode of 240 nm under cirrus cloud conditions, using a continuous-flow diffusion chamber. The authors reported that these coated soot particles require RH_i values of 152 % and 156 %, respectively, to reach the

1 % AF level at 228 and 223 K (DeMott et al., 1999), which is close to the RH_i values of 152 % and 154 % at the same T for 200 nm mCASTblack soot particles with thick H_2SO_4 coatings presented in this study. It is reported that soot particles with aggregate compaction after experiencing a cloud process can nucleate ice via PCF at RH < RH_{hom} conditions when $T <$ HNT (Mahrt et al., 2020b). However, even though the thick H_2SO_4 coating of the mCASTblack soot particle in this study results in significant size shrinkage (see Fig. 3a and b), i.e. some extent aggregate compaction (see Figs. 8c and 9c), its ice nucleation ability is not promoted compared to the uncoated particles. This suggests that the availability of pores (i.e. pore volume) without a freezing depression will be a prerequisite for PCF ice nucleation despite lowering the soot–water contact angle by H_2SO_4 coating.

3.2 H_2SO_4-coated FW200 soot ice nucleation results

In general, H_2SO_4 coating has limited effects on FW200 soot particle droplet activation ability at $T >$ HNT as shown in Figs. 6 and 7. There is no significant deviation between the AF curves of soot particles (both for 200 and 400 nm) with and without H_2SO_4 coating at 243 and 238 K. It is safe to conclude that the H_2SO_4 coating generated in this study does not enhance FW200 soot particle water interaction and CCN activation ability at these two Ts. The AF curves of bare
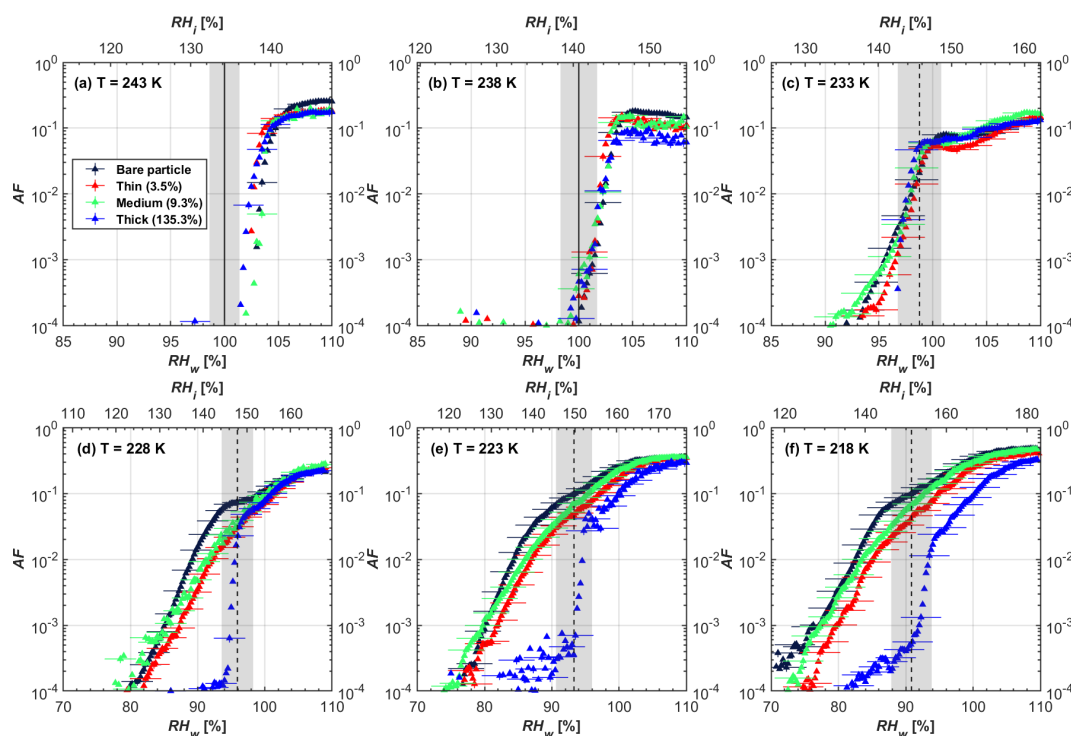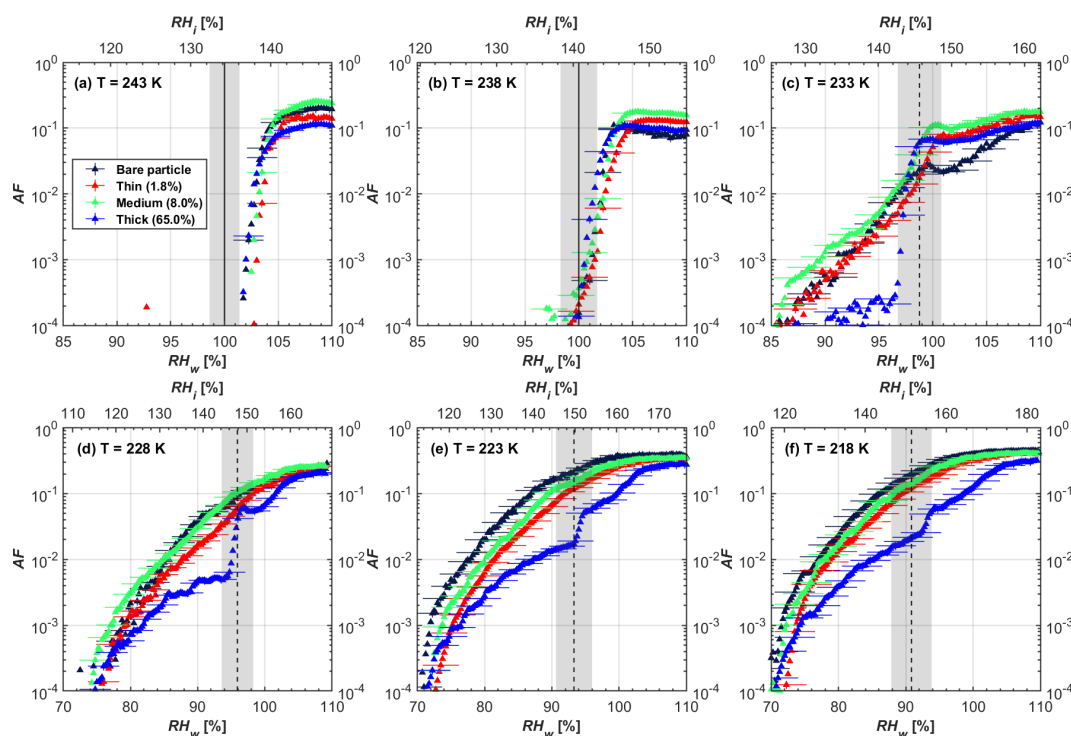
Figure 6. AF as a function of RH at the given temperatures for 200 nm FW200 soot particles. Black solid lines represent water saturation conditions according to Murphy and Koop (2005). Black dashed lines denote the expected RH values for solution droplet homogeneous freezing at $T <$ HNT (Koop et al., 2000). The grey-shaded area shows the possible RH variation and uncertainty in HINC for the calculated water saturation and homogeneous freezing conditions. The percentages represent the H_2SO_4 coating wt %.

and coated FW200 soot particles in Figs. 6 and 7 are consistent with the study conducted by Koehler et al. (2009), who reported that the CCN activation of hydrophilic aviation kerosene soot particles requires higher RH conditions than the Kelvin RH limit (Henson, 2007), which is required by wettable particles to show CCN activation. We attribute our results to the absence of a uniform H_2SO_4 coating similar to that discussed above. With such a non-uniform coating, the hygroscopicity of coated H_2SO_4 does not exhibit its water interaction enhancement for its host soot particle.

From the AF curves in Figs. 6 and 7 at $T <$ HNT, thinly and moderately coated FW200 soot particles form ice crystals at RH $<$ RH_{hom}, showing that PCF is still well preserved. This means pores or voids with the right size for PCF are not all blocked or are still available when soot particles are coated by H_2SO_4, also implying that the adsorbed H_2SO_4 by the soot particle does not distribute evenly or uniformly. In general, thin and moderate H_2SO_4 coatings cannot depress FW200 soot ice nucleation ability for both 200 and 400 nm coated FW200 soot particles. At $T <$ HNT, the 200 nm soot particles with thick H_2SO_4 coverage show an obvious ice activation depression and an apparent freezing mechanism shift from PCF to homogeneous freezing near the homogeneous freezing RH thresholds, as shown in Fig. 6. Thickly coated 400 nm FW200 soot particles in Fig. 7 show a simi-

lar ice nucleation onset compared to bare soot particles but with a slight suppression in total AF observed, suggesting the ice nucleation mesoporous volume for PCF is still available. Approaching RH_{hom}, there is a clear shift in the slope of the AF curves at $T \leq 233$ K in Fig. 7, suggesting a mechanism change from PCF to bulk homogeneous freezing, which aligns with the predictions of Koop et al. (2000). Overall, 200 nm soot particle ice nucleation abilities are more affected by the thick H_2SO_4 coating compared to 400 nm particles. Given the approximate spherical structure of a FW200 soot aggregate containing a group of coalesced primary particles, a larger size and surface area will require a higher H_2SO_4 coating wt % to achieve the same equivalent coating coverage as that of a smaller aggregate. Soot particles with a small mobility diameter (e.g. 200 nm) contain less pore volume and can be more easily covered by H_2SO_4 coatings, and thus their PCF activation is readily inhibited and they freeze homogeneously like a H_2SO_4 droplet with a soot particle core. It is safe to extrapolate that further H_2SO_4 coating for 200 nm FW200 soot particles will totally depress its PCF freezing tail (at 218 K) and that the coated particle will freeze only homogeneously according to Koop et al. (2000). Comparably, 400 nm FW200 soot particles contain more abundant pore structures which are not inhibited to PCF even upon excessive H_2SO_4 coating. For the same H_2SO_4 coating wt %, more

Figure 7. AF as a function of RH at the given temperatures for 400 nm FW200 soot particles. Black solid lines represent water saturation conditions according to Murphy and Koop (2005). Black dashed lines denote the expected RH values for solution droplet homogeneous freezing at $T <$ HNT (Koop et al., 2000). The grey-shaded area shows the possible RH variation and uncertainty in HINC for the calculated water saturation and homogeneous freezing conditions. The percentages represent the H_2SO_4 coating wt %.

PCF active pores are available in 400 nm FW200 soot particles than in 200 nm particles. This again implies that the distribution of H_2SO_4 onto soot particle surfaces is not uniform or that the H_2SO_4 coating states are different over soot particle local structures.

To sum up, we propose three possible scenarios to explain the H_2SO_4 coating effects on mCASTblack and FW200 soot particle IN activities. Firstly, H_2SO_4 may fill in and block some mesopores of the soot aggregate, making it PCF inactive at low T because the subsequent porewater capillary condensation into H_2SO_4-filled pores will form concentrated H_2SO_4 solutions with a low homogeneous nucleation rate (Koop et al., 2000). This can be attributed to thin or medium H_2SO_4 coating wt % scenarios for mCASTblack. Meanwhile, if the soot particle is porous and contains sufficient pore structures, some mesopores can remain unfilled and are still able to induce PCF such as for thin and medium coatings of 200 nm FW200 and even for a thick coating of 400 nm FW200. Secondly, most of the mesopores are affected by H_2SO_4. Under low RH conditions, mesopores filled with H_2SO_4 solution require a higher saturation condition to freeze in order to recover to high enough water activity and to compensate for the homogeneous nucleation rate depression. Under higher RH conditions near a homogeneous freezing condition, the depressed PCF mechanism

is not active, and so these coated particles freeze homogeneously. The second scenario can help with the understanding of thick H_2SO_4 coating effects on mCASTblack particles and 200 nm FW200 particles. Finally, excessive H_2SO_4 coating tends to block all pores and shuts down the PCF mechanism. In this case, H_2SO_4 might form a shell on the particle surface or encapsulate the particle, so the coated particle behaves as a H_2SO_4 droplet and only freezes via homogeneous freezing. We suggest that the last scenario is relevant to soot particles with high H_2SO_4 coating wt % ($> 100\%$). Detailed descriptions of these three coating states will be given in Sect. 3.3.2.

3.3 Typical internally mixed states of soot particles and sulfuric acid

Here we use the single particle size and mass results coupled with microscopy of the particle mixing state and the ice nucleation activities of H_2SO_4-coated soot particles to propose a hypothesis on the internal mixing state of H_2SO_4 and soot particles. In this section, particle microscopy characterization results will be presented first, and next a three-step process for soot particle H_2SO_4 coating will be explained to further understand particle ice nucleation activities shown in Sect. 3.1 and 3.2.

3.3.1 SEM, TEM and EDX results to characterize particle morphology

SEM results for both bare and coated soot particles are shown in Fig. 8. These SEM images are taken at 200 k magnification for 400 nm mCASTblack and FW200 soot particles with H_2SO_4 coating wt % similar to those coated soot particles in Figs. 5 and 7 and also termed bare, thin and thick coatings. Images for the same soot samples at 20 k magnification are provided in Fig. C1. As seen in Fig. 8a, bare 400 nm mCAST-black soot particle is fractal and looks like a long primary particle chain with lacy voids. Thinly coated 400 nm soot aggregate (as shown in Fig. 8b) is close to the bare aggregate. Some primary particles form a chunk with thick H_2SO_4 coating, and the shape of the primary particles is more ambiguous than in the bare aggregate, which can be seen in Fig. 8c (thick coatings). In addition, thickly coated 400 nm mCAST-black soot aggregates tend to collapse by showing a more compacted and less fractal 2D projection shape compared to bare and thinly coated aggregates.

Figure 8d shows that a FW200 bare 400 nm soot aggregate is less fractal than the same-sized bare mCASTblack soot aggregate in Fig. 8a. This is in agreement with the particle fractal dimension results presented in Mahrt et al. (2018), where the authors reported a higher fractal dimension value for the FW200 soot particle (2.35) compared to mCAST-black (1.86). The particle fractal dimension is used to quantitatively describe soot particle morphology, considering that the number of primary particles scales as a power law with the radius, and thus a chain agglomerate would have a fractal dimension of 1 and a sphere of primary particles would have a fractal dimension of 3. There are no distinguishable morphological feature differences between Fig. 8d and e, which means that thin H_2SO_4 coating does not result in a significant soot surface topography change with a 1.8 % H_2SO_4 coating mass. We believe that a small amount of H_2SO_4 first fills into pores among primary particles and is unable to modify the particle surface significantly. However, heavier mass coatings will have a part of the soot aggregate embedded in the H_2SO_4 material, as is clearly visible in Fig. 8f. These images are comparable to the SEM images for ambient soot particles in a field study (Bhandari et al., 2019; see Fig. S4b). Besides, a ring of spray in Fig. 8f is demonstrated to be small H_2SO_4 droplets resulting from the impaction (Virtanen et al., 2010) of soot aggregates on the Cu grid, as seen in EDX results (discussed below and see Fig. 11). Similar results about H_2SO_4 coating introducing morphology change for FW200 soot can also be seen from the TEM images shown in Fig. C2f.

TEM images of 200 nm bare and thinly and thickly coated for both mCASTblack and FW200 soot particles are shown in Fig. 9. The coating wt % is presented in Table 2 and is similar to those of the ice nucleation experiments, as mentioned before in Sect. 2.2.3. There is no apparent morphology difference between bare and thinly coated aggregates for mCASTblack soot (as shown in Fig. 9a and b), which
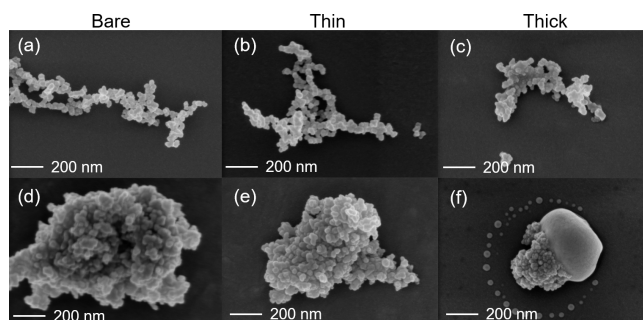

Figure 8. SEM images (Zeiss Leo 1530, Signal = InLens, EHT = 3 kV) for 400 nm size-selected bare and coated mCAST-black and FW200 soot particles. Scale bars are indicated in each image. **(a)** Bare mCASTblack, **(b)** mCASTblack with a thin coating (coating wt = 1.9 %), **(c)** mCASTblack with a thick coating (coating wt = 31.1 %), **(d)** bare FW200, **(e)** FW200 with a thin coating (coating wt = 1.8 %), and **(f)** FW200 with a thick coating (coating wt = 65.0 %).

is consistent with the SEM results. However, the aggregate size in Fig. 9a and b is much larger than 200 nm. This could be an artifact during grid sample collection, which results in soot-aggregate piling or agglomeration when particles deposit onto the grid. Small aggregates can also coagulate while transporting in the aerosol flow (Kulkarni et al., 2011). In addition, soot aggregates are of heterogeneous shapes, and even size-selected monodisperse soot aerosol spreads larger than the selected size. Besides, a part of double-charged particles, which have a larger mobility diameter, also exist, as already specified in Sect. 2.2.3 (see Fig. A3). Thus, these larger aggregates with higher inertia are more effectively collected by ZEMI. Nevertheless, the aggregate in Fig. 9a or b is already much larger than the size of a double-charged 200 nm aggregate (∼ 320 nm). In order to support the large aggregate sizes being an artifact of grid sampling, the optical sizes of suspended soot aggregates for TEM grid collection are also tested by the OPC, and the results are presented in Appendix C, showing that the suspended aggregates are binned into the expected optical size channels and demonstrating that their size selection is acceptable. The thickly coated mCASTblack aggregate in Fig. 9c shows a more compacted 2D projection shape, which suggests that the thick coating increases primary particle connectivity, resulting in aggregate collapse. Similarly to mCASTblack, thin H_2SO_4 coating for FW200 soot particles does not lead to distinguishable features, comparing Fig. 9d to Fig. 9e. Clearly, a thick coating for FW200 soot particles results in a more collapsed aggregate projection, with the edge boundary being smoother than the bare and thinly coated ones (see Fig. 9f). This process of soot-aggregate collapse can also be explained by the decrease in mobility diameter of soot particles with thick coatings shown in Fig. 3c. In addition, thick H_2SO_4 coating seems to show a darker visualization effect for FW200 soot aggregates compared to bare particles. In addition, TEM images provide ev-
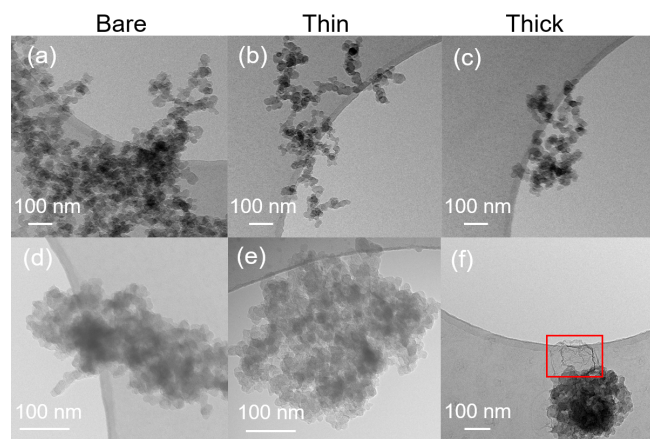
Figure 9. TEM images for 200 nm size-selected bare and coated mCASTblack and FW200 soot particles. Scale bars are indicated in each image. **(a)** Bare mCASTblack, **(b)** mCASTblack with a thin coating (coating wt = 2.9 %), **(c)** mCASTblack with a thick coating (coating wt = 30.2 %), **(d)** bare FW200, **(e)** FW200 with a thin coating (coating wt = 2.3 %), and **(f)** FW200 with a thick coating (coating wt = 139.3 %). Microscopes used: **(a)**–**(c)** and **(f)** TFS F30, **(d)** and **(e)** Hitachi HT7700.

idence of H_2SO_4 presence on soot particle surfaces, which is consistent with SEM images. In Fig. 9f, the watermark indicated by a red square between the particle and the edge of the carbon support film is believed to be a H_2SO_4 footprint. During the electron microscopy it could be observed how the structure, which looked initially like a balloon, slowly evaporated and finally left this shrivelled skin. Evidence of the presence of H_2SO_4 on soot primary particle surfaces and H_2SO_4 pore-filling effects from HR-TEM images is presented in the Appendix, Figs. C4 and C5.

EDX measurements demonstrated that H_2SO_4 coating has a non-uniform distribution on soot-aggregate surfaces. Grids with 200 nm mCASTblack and FW200 soot aggregates are sampled. To characterize the soot-aggregate surface H_2SO_4 distribution, composite images in the HAADF (high-angle annular dark field) of 2D EDX elemental maps for S (red dots in Figs. 10a and 11a) are used. With a focus on the particle surface chemical composition, C, O and S element contents for areas of interest (AOI) within a soot-aggregate projection are quantified to obtain the spectra to avoid the influence of grid material, as indicated by the red square in Figs. 10a and 11a. The mass percentage of each element is normalized by the total result of these three elements and is attached in Figs. 10b and 11b. Background signal-corrected element spectrum results are provided in Appendix C.

Comparing S maps for mCASTblack in Fig. 10a, the presence of H_2SO_4 on the soot is indicated by an increasing signal level with increasing coating thickness. However, the coating material distribution is not uniform on the soot-aggregate surfaces. A radar chart in Fig. 10b shows quantitative chemical composition changes for H_2SO_4-coated

mCASTblack soot. With H_2SO_4 coating, the S content increases as expected, whereas the O content decreases, which is unexpected because H_2SO_4 contains a significant proportion of oxygen. This may suggest that there is a reaction between mCASTblack soot and H_2SO_4 depleting some O content in the process, considering H_2SO_4 to be a strong oxidant with respect to mCASTblack soot (Mahrt et al., 2020b). From the table in Fig. 10b, even though thick coating has a H_2SO_4 coating mass percentage by more than 30 %, only a tiny amount of S is detected by the EDX measurement over AOI. It is feasible that the soot local surface (i.e. AOI) detected has a lower coating wt % than the global soot particle considering non-uniform H_2SO_4 coating distribution on the soot surfaces. Additionally, a part of the H_2SO_4 coating material is lost during the measurement because of the heating effect from high-energy electron beams, which also partly explains the lower H_2SO_4 content detected by EDX mapping. In Fig. 11a for FW200 soot, intensive S signals (red markings) on coated particle surfaces also suggest random distribution of coating material and that there are preferred sites for the interaction of soot and H_2SO_4. Red markings for S attached with and distributed around thickly coated soot aggregate are shown to be the footprint of H_2SO_4 droplets. This finding coincides with the SEM result in Fig. 8f and the TEM result in Fig. 9f. The normalized C, O and S mass ratio result clearly suggests the increment of the H_2SO_4 coating material in terms of O and S and the decreasing share of soot material in terms of C (Fig. 11b). In contrast to coated mCASTblack soot particles, the normalized proportion of O in H_2SO_4-coated FW200 soot particles increases with higher H_2SO_4 coating wt %, suggesting that H_2SO_4 coating-induced surface reaction (or oxidation) for FW200 soot does not occur (or at least not to the same extent) like that for mCASTblack soot. This can be attributed to the fact that FW200 soot is already surface oxidized during its production according to the information provided by the manufacturer (see Table 1 in Mahrt et al., 2018).

Overall, SEM images show that thick H_2SO_4 coatings may change soot-aggregate surface topography. Likely, the coating material can either be distributed over the soot surfaces unevenly and change the connectivity of adjacent primary particles or will pile up over primary particle clusters to form chunks and finally form a H_2SO_4 shell. TEM images show that thin H_2SO_4 coatings do not change the morphology of soot aggregates, whereas thick H_2SO_4 coatings can modify their morphology significantly by inducing aggregate structure compaction. EDX 2D maps provide robust evidence of the presence of H_2SO_4 over soot aggregates and further demonstrate that the H_2SO_4 distribution is not uniform. Comparing the thick coating results for 200 nm mCASTblack soot (Fig. 9c) to those of FW200 soot (Fig. 9f), coating effects on mCASTblack soot-aggregate morphology modification are different even though the coating-equivalent ML values are similar (3.4 ± 0.4 and 3.6 ± 0.3 ML, respectively, according to Table 2). Moreover, the SEM image with
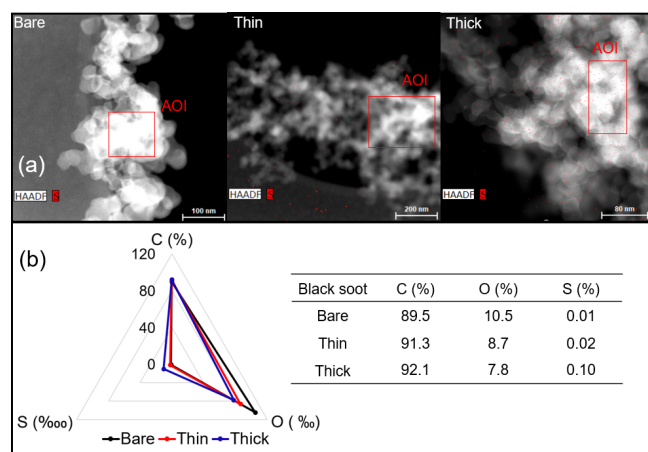
Figure 10. Panel **(a)**: 2D EDX maps for sulfur (S) on 200 nm mCASTblack bare, thinly coated (coating wt = 2.9 %) and thickly coated (coating wt = 30.2 %) aggregates. Sulfur signal (red dots) is overlain on HAADF (high-angle annular dark-field) images. Scale bars are indicated in each image. Panel **(b)**: the normalized carbon (C), oxygen (O) and S mass percentage of the areas of interest (AOI, indicated as the red square in panel **a**) for mCASTblack soot with different coating thicknesses.
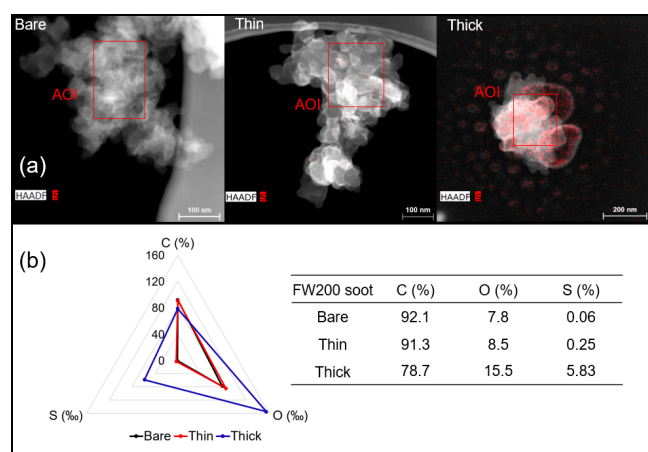

Figure 11. Panel **(a)**: 2D EDX maps for sulfur (S) on 200 nm FW200 bare, thinly coated (coating wt = 2.3 %) and thickly coated (coating wt = 139.3 %) aggregates. Sulfur signal (red dots) is overlain on HAADF images. Scale bars are indicated in each image. Panel **(b)**: the normalized carbon (C), oxygen (O) and S mass percentage of the AOI (indicated as the red square in panel **a**) for FW200 soot with different coating thicknesses.

a higher 3.5 equivalent ML coating for 400 nm mCASTblack aggregate (Fig. 8c) compared to that of a 400 nm FW200 aggregate with 1.7 equivalent ML coating (Fig. 8f) does not show more compaction of mCASTblack particles. This different coating effect between mCASTblack and FW200 soot results from the differences in intrinsic soot morphology properties. Nonetheless, we expect that mCASTblack soot aggregates can also be embedded in H_2SO_4 and appear to
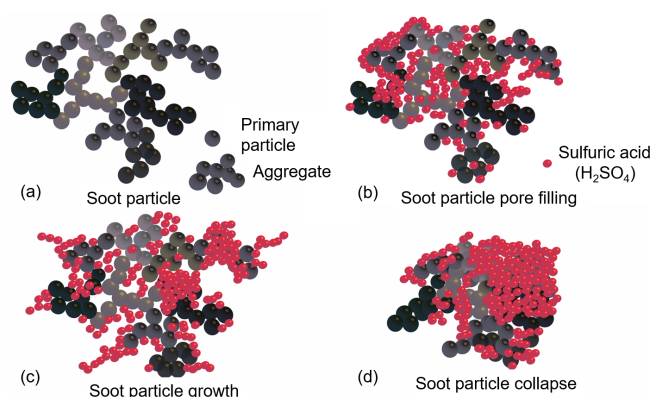
Figure 12. Illustration of the proposed H_2SO_4 coating processes for soot particles (not to scale). Bare soot particle **(a)** and soot particle pore filling and surface coating induced by progressive increase in H_2SO_4 coating mass (**b, c, d**).

be as compacted as thickly coated FW200 if H_2SO_4 coating wt % is achieved, e.g. > 100 %. Therefore, the equivalent ML value is not a reliable proxy to describe the distribution of H_2SO_4 coating material on soot-aggregate surfaces.

3.3.2 A three-step process for soot particle H_2SO_4 coating

Based on the aforementioned soot particle ice nucleation activity and property characterization results, we hypothesize that the soot coating process presented here has three stages (as illustrated in Fig. 12). A soot aggregate comprising numerous primary particles has a complex intra-aggregate structure (Vander Wal et al., 2007; Bond et al., 2013), a sketch of which is shown in Fig. 12a. We first start with a small amount of H_2SO_4 coating (Fig. 12b) where H_2SO_4 molecules fill into pores among primary particles or voids in the soot aggregate because of the capillary force, but not all pores will be filled completely. Meanwhile, H_2SO_4 molecules can form clusters (humps or small islands) on the surfaces. At this point, the particle size is not expected to change, as supported by the single particle mass and size results shown in Fig. 3. The particle effective density increases following a smooth slope, showing the gain of H_2SO_4 as the density of bare soot particles is smaller than that of pure H_2SO_4. In general, the overall coating effect of the first stage is pore filling and, if any, some aggregate shrinking.

Further increase in coating mass results in a more complete pore filling and the spread of H_2SO_4 on aggregate surfaces. As depicted in Fig. 12c, at this stage of the coating process, particle size growth starts to be detectable. At this stage, the particle effective density may increase in a different manner depending on soot types. In Fig. 3, mCASTblack soot particle effective density does not change, whereas FW200 soot effective density continues to increase. This is because mCASTblack soot is more fractal or lacy (Figs. 8 and 9)

and H_2SO_4 may form molecule clusters or branches sticking on the particle surfaces. Hence, the size growth effect overwhelms the mass increase effect. By contrast, FW200 soot is more compact and has abundant pore structures, and thus H_2SO_4 can be accommodated inside the pore volume. Thus, the addition of H_2SO_4 for FW200 soot shows a lower size growth effect than for mCASTblack soot. Therefore, the main effect of the second stage in the H_2SO_4 coating process is further pore filling with coating material spreading to the surfaces. Very likely, H_2SO_4 shows preference for the soot particle surfaces and will firstly stick to some special sites on the surface before forming molecule clusters. For example, Garland et al. (2008) used SEM and atomic force microscopy (AFM) to investigate how the oleic acid deposits on soot particle surfaces and suggested that oleic acid islands with a height of several nanometres will be accumulated on the surface rather than form a uniform oleic acid coverage layer.

Finally, once pores are filled and the growth of the H_2SO_4 cluster on the surface continues, the growing H_2SO_4 clusters will interact with each other or collapse onto the particle surfaces, or neighbouring islands start to merge into big patches. This process also induces collapse of the particle structure causing particle compaction, as shown in Fig. 12d. Some researchers suggested that soot compaction occurs during the condensation or addition of coating materials (Hallett et al., 1989; Tritscher et al., 2011; Schnitzler et al., 2017) because the coating material exerts capillary forces between coating monomers, leading to soot-aggregate restructure and a more compact morphology. Consequently, the third mixing state results in the particle collapse and finally forms H_2SO_4-encapsulated particles with a soot core if the coating is thick enough. This argument is supported by the more compacted morphology of thickly coated soot particles (see Figs. 8f and 9f) in SEM and TEM images showing particles embedded or partially embedded in H_2SO_4 droplets. Such a mechanism is also supported by some work in the literature. For example, fractal soot agglomerates can be compacted by the condensation of ozonolysis products of α-pinene secondary organic aerosol (SOA) with the bare soot particle serving as a nucleation centre (Saathoff et al., 2003). Khalizov et al. (2009) also pointed out that small soot aggregates gain size growth but larger aggregates show size shrinkage, i.e. partial soot-aggregate collapse, due to structure compaction after being exposed to gaseous H_2SO_4 for more than 10 s. Most recently, Pei et al. (2018) investigated the morphological changes in soot particles after H_2SO_4 or limonene ozonolysis SOA coating and suggested that the coating material will change soot particle nanostructure by a two-step process. Firstly, external coating material will fill into the voids or pores among soot aggregates. Next, the particle size will grow with further vapour condensation when the voids are filled completely. In brief, our three-stage hypothesis can be supported by measurements in this study and is also in agreement with previous findings in the literature.

4 Atmospheric implications

Soot particles in the troposphere can affect cirrus cloud formation. H_2SO_4 coatings have a clear suppression effect on soot particle ice nucleation based on the extent of the coating and the soot particle properties, with compact and porous particles being able to resist suppression in ice nucleation more than fractal particles. The difference in this suppression effect is because of the higher availability of mesopores in compact soot particles. Given the long lifetime (from a ~ 5 d global mean up to 3 weeks) of soot particles in the atmosphere (Liu, 2005; Shen et al., 2014; Lund et al., 2018; Liu et al., 2020), the processes soot particles undergo with respect to aging and cloud processing can be complex (see examples in Kanji et al., 2017). Due to the ubiquitous nature of H_2SO_4 in the troposphere (Pye et al., 2020), acid coatings are likely atmospheric aging processes for soot particles. Hence, it would be important to consider the sulfate–soot mixing state when evaluating the impact of soot on cirrus cloud formation. As demonstrated in this study, soot particles internally mixed with H_2SO_4 exhibit a suppressed ice nucleation ability depending on their size and morphological properties. Thick H_2SO_4 coatings (wt % > 100 %) effectively make the soot ice nucleation contribution to cirrus cloud formation comparable to homogeneous freezing of solution droplets. Therefore, the soot–sulfate mixing state impact on ice nucleation should be considered in predicting the impact of soot particles on cirrus formation as well as when evaluating the radiative forcing and climate impacts of ice clouds in the upper troposphere (Lohmann et al., 2020). In other words, using soot proxies without sulfate coatings may only be relevant for regions where soot is quickly incorporated into the cloud upon emission. Field studies detected soot aggregates with 0.1–1 μm sizes in ice crystal residuals sampled from cirrus clouds (Petzold et al., 1998; Twohy and Poellot, 2005; Cziczo and Froyd, 2014), and the presence of 100–800 nm BC particles in the interstitial aerosol samples increases with increasing altitude from 8 to 11 km in the cirrus cloud regime (Petzold et al., 1998). Soot particles emitted from biomass burning and aviation activities are dominated by fine particles (< 100 nm) in number concentration; however, large particles (> 100 nm) dominate in volume concentration (Brito et al., 2014; Fushimi et al., 2019). In addition, X. Zhang et al. (2020) reported that fine particles coagulate into large soot aggregates downstream of the emission upon aviation plume evolution. Thus, we believe that the results presented in this study are of atmospherically relevant sizes (200 and 400 nm).

Considering that mCASTblack soot represents fractal and hydrophobic soot (Marhaba et al., 2019) and as an appropriate proxy for aviation soot particles (Ess and Vasilatou, 2018), H_2SO_4-coated mCASTblack soot particles in this study can be comparable to aviation soot particles coated by H_2SO_4 in the atmosphere. At $T <$ HNT, H_2SO_4-coated aviation soot particles may not inhibit or compete with droplet

homogeneous freezing. This is because bare and H_2SO_4-coated 200 and 400 nm mCASTblack particles freeze under conditions for homogeneous freezing of solution droplets. Despite the minor ice nucleation ability of mCASTblack soot via PCF even at 218 K as presented in this study, uncoated aviation soot analogous to fractal and hydrophobic mCAST-black may still influence cirrus cloud properties if soot particles are at present in sufficiently high number concentrations near their sources because a non-negligible number will nucleate ice crystals (Kärcher et al., 2021). Moreover, the PCF activation of mCASTblack soot particles with a low H_2SO_4 coating wt % will be further depressed and require $RH > RH_{hom}$ conditions to form ice crystals. This implies that aviation soot particle proxies even with a low H_2SO_4 coating mass (similar to the mCASTblack soot low-H_2SO_4 coating wt % presented in this study) could only form ice crystals above RH_{hom} conditions at $T < HNT$.

Initially active soot particles (similar to the FW200 soot sample used in this study), if not extensively mixed with H_2SO_4 in the atmosphere, only demonstrate a slight suppression in ice nucleation ability at cirrus-relevant temperatures ($T < 233$ K). Thus, these coated particles still nucleate ice via PCF, forming ice crystals under $RH < RH_{hom}$ conditions, with the potential to perturb the cirrus background. Thickly coated soot particles, freezing homogeneously, are also atmospherically relevant. Bhandari et al. (2019) collected ambient soot particles under different weather conditions in a valley and reported that most ambient soot particles are covered with a thick coating or are embedded in external materials. If these thickly coated soot particles can be activated as droplets and transported to high altitudes under lower T conditions, they likely nucleate ice homogeneously. Under water-supersaturated conditions at $T < HNT$, it is reported that the homogeneous freezing of water-activated soot particles is the dominant ice crystal formation pathway for cirrus clouds (Kärcher and Yu, 2009). Consequently, the water interaction enhancement of soot particles with thick H_2SO_4 coatings in this study resembles this case. According to Ditas et al. (2018), BC particles emitted by wildfires can reach the lowermost stratosphere, and the authors suggested that a BC particle with a 120 nm average mass equivalent diameter can be coated by volatile organic compounds (VOCs) and/or H_2SO_4 with a thickness of 150 nm. In this case, our findings imply that homogeneous freezing will be the dominant mechanism for ice nucleation as even the very active FW200 soot particles lose their ice nucleation ability with such a thick H_2SO_4 coating. As such, knowing the aging history (trajectory) of soot particles in the upper troposphere would be crucial for accurately determining the role of soot particles in cirrus cloud formation. Mahrt et al. (2020b) suggested that cloud-processing-induced aggregate compaction of soot samples significantly enhances their ice nucleation ability in the cirrus cloud regime. However, no enhancement or even a suppression of ice nucleation ability is to be expected in the cirrus cloud regime if the compaction arises

from thick coatings of H_2SO_4 and PCF-relevant pore structures become unavailable.

In brief, H_2SO_4 coating modifies soot particle ice nucleation in the cirrus cloud regime by decreasing the pore availability for PCF activation, thereby inhibiting ice formation below RH_{hom} conditions. This finding is consistent with a model simulation study based on the soot–PCF framework (Marcolli et al., 2021) performed by Kärcher et al. (2021), who reported that only barely coated soot particles larger than ~ 100 nm with sufficient mesopore structures can contribute to cirrus cloud ice formation. Nonetheless, the authors also suggested that even a small number of active uncoated soot particles (~ 11 L^{-1}) can decrease the total number of cirrus ice crystals but increase the ice crystal mean size by forming ice via PCF processes while competing with the homogeneous freezing of aerosol droplets (Kärcher et al., 2021). Therefore, soot particles may still play an important role in regulating cirrus cloud properties, despite the suppressed ice nucleation ability caused by H_2SO_4 coating.

5   Summary

The ice nucleation ability of two samples, an organic-poor (mCASTblack) and a porous commercial carbon black (FW200) soot, were investigated. The soot particles coated with H_2SO_4 to different degrees are systemically studied at $T = 243$–218 K under RH conditions from ice saturation to well above water supersaturation. Auxiliary measurements for soot sample property characterization, including particle mobility diameter and mass, H_2SO_4 coating wt %, soot-aggregate morphology and surface chemical composition, were performed. Overall, H_2SO_4 coating on soot particles can modify soot-aggregate morphological properties depending on the coating wt % and enhance soot–water interaction ability, thereby impacting soot particle ice nucleation abilities. For $T > HNT$, i.e. in the mixed-phase cloud regime, soot particles with/without H_2SO_4 coating do not nucleate ice. The C_3H_8 flame fuel-lean soot (mCASTblack), viewed as an aviation soot proxy in laboratory studies, is originally a poor INP at $T < HNT$. High wt / wt % H_2SO_4-coated 200 and 400 nm mCASTblack soot particles form ice crystals via homogeneous freezing, and low wt / wt % H_2SO_4 coating even depresses their ice nucleation to $RH > RH_{hom}$ conditions at $T < HNT$. Porous FW200 bare soot particles and FW200 soot particles with thin or moderate H_2SO_4 coating can nucleate ice crystals via PCF below homogeneous freezing conditions at $T < HNT$. However, thick H_2SO_4 coatings exert a size-dependent effect suppressing small-sized (200 nm) FW200 soot PCF activation more than that of larger-sized particles (400 nm). Thickly coated 200 nm particles freeze homogeneously, requiring a smaller H_2SO_4 coating wt % than that for 400 nm particles. Based on the above results, we propose a three-step H_2SO_4 coating process on soot aggregates with increasing H_2SO_4 coating masses, inclusion of pore filling,

H_2SO_4 spreading over soot particle surfaces and soot particle structure collapse.

The findings in this study have implications for the ice nucleation of smaller-sized soot particles (< 100 nm). The understanding of the lower size threshold for soot ice formation is important, given the strong particle size dependence of (soot) ice nucleation and that the Aitken mode dominates size distribution from aviation soot emissions and other high-temperature combustion sources. A recent study reported that small-sized (< 100 nm) soot particles, even as active as uncoated FW200 in this study, nucleate ice homogeneously for $T <$ HNT (Gao et al., 2022a), implying that H_2SO_4-coated soot particles of a size smaller than 100 nm require homogeneous freezing conditions to form ice in the cirrus cloud regime. Moreover, this study contributes to the climate impact evaluation of soot emissions. Despite the various coating thicknesses in the atmosphere, a thin H_2SO_4 coating ($\leq$ monolayer coverage) onto soot particles can lead to suppressed ice nucleation. As such, the aerosol–climate model may only need to differentiate between coated and uncoated soot particles when evaluating the H_2SO_4 coating effects on soot ice nucleation abilities, as a monolayer of sulfuric acid coating can easily be achieved in the atmosphere (Pósfai et al., 1999; Adachi et al., 2011). As demonstrated in this study, H_2SO_4 coating changes soot particle morphology and modifies its water interaction ability simultaneously. Differentiating between these two coating effects to identify the dominant effect on ice nucleation is still an open question for future studies. In addition to H_2SO_4 coating, atmospheric aging altering soot particle ice nucleation abilities can include chemical oxidation, organics coating and clouding processing in the atmosphere. Only a small proportion of studies in the literature have examined these topics systematically. Experimental studies on these soot aging processes will benefit the understanding of the role of soot in cirrus cloud formation.

Appendix A: The mixing state of soot and H_2SO_4

In order to ensure the absence of pure nucleated H_2SO_4 particles in the mixing state aerosol flow, the particle size distribution evolution of the aerosol in the coating apparatus was measured. Here, we present the internal mixing process of 200 nm mCASTblack soot with a H_2SO_4 coating wt % = 15.6 % as an example. As shown in Fig. A1, particle size distribution for the 0 min state of pure H_2SO_4 aerosol in the coating apparatus (red line) and 200 nm size-selected bare soot particles (black dashed line) were conducted firstly and respectively. Afterwards, 200 nm mCASTblack bare soot aerosol was fed into the coating apparatus. The mixed aerosol particle size distribution was monitored until it reached a stable state (20 min black line, Fig. A1). In addition, a comparison between the aerosol particle mass distribution of bare soot particles and H_2SO_4-coated particles was made to fur-
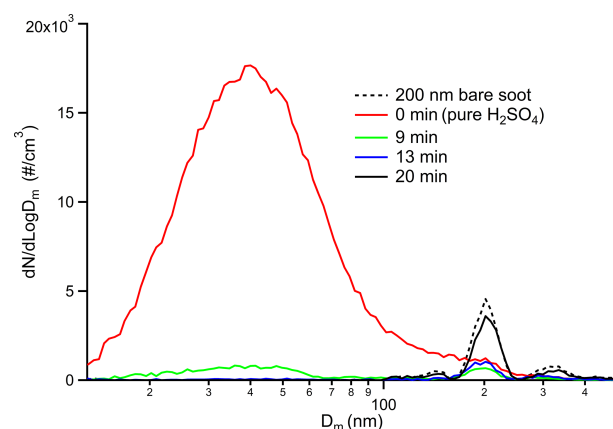
Figure A1. The raw size distribution of the particles coming out of the coating apparatus in 20 min after 200 nm mCASTblack soot aerosol sample flow is connected to the coating apparatus. The red line denotes the initial state of H_2SO_4 aerosol, where only nucleation-mode H_2SO_4 exists in the coating system without soot particles. The dashed black line indicates bare 200 nm black soot particles. The green line presents the particle size distribution 9 min later when the soot particles were fed into the coating apparatus. The blue line shows the particle size distribution 13 min later. The black line stands for the stable mixing state of soot particles with H_2SO_4.
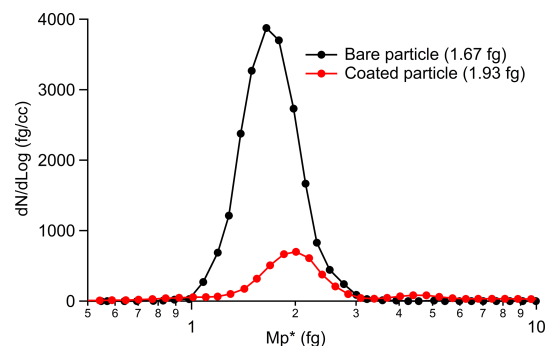

Figure A2. The raw data mass distribution of 200 nm mCAST-black soot bare particles and H_2SO_4-coated particles. The black line shows the mass distribution of bare particles with a mass-mode value of 1.67 fg derived from the log-normal distribution. The red line presents the mass distribution of H_2SO_4-coated particles with a mass-mode value of 1.93 fg.

ther demonstrate that pure nucleated H_2SO_4 particles are absent in the aerosol flow produced from the coating apparatus (Fig. A2).

Figure A1 depicts the particle size distribution evolution process of the mixing state of soot particles with H_2SO_4. At the very beginning of the measurement, pure nucleated H_2SO_4 aerosol shows a high particle number concentration and a small-sized distribution with a mode peak at ~ 40 nm. After 200 nm bare soot particles are introduced into the coating apparatus for several minutes, and the mixed aerosol
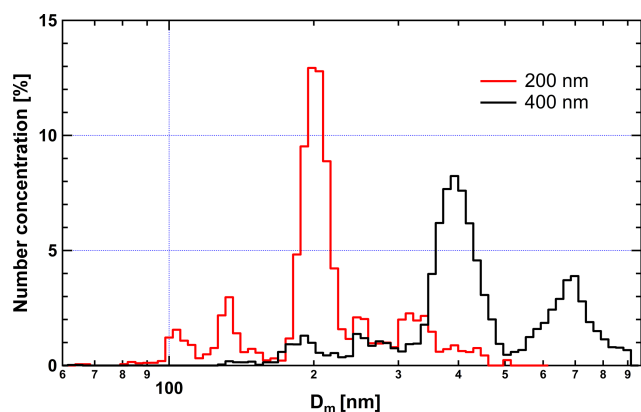
Figure A3. Number size distribution in terms of particle concentration percentage as a function of mobility diameter (D_m) for 200 and 400 nm size-selected mCASTblack bare soot particles.
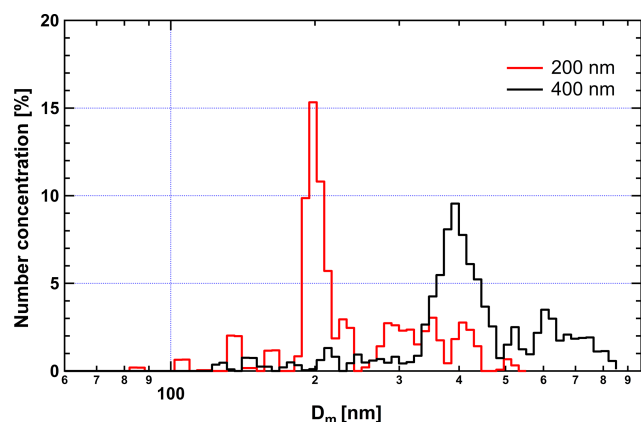

Figure A4. Number size distribution in terms of particle concentration percentage as a function of mobility diameter (D_m) for 200 and 400 nm size-selected FW200 bare soot particles.

particle number concentration dramatically decreases. With more time, the pure H_2SO_4 particle size distribution mode is absent and a size distribution peak around 200 nm becomes more distinct, indicating that the mixing state of soot particles and H_2SO_4 is changing over time. Finally, the size distribution of the mixed particles reaches a stable state as shown in the figure denoted by solid black line. Comparing the bare (dashed black line, Fig. A1) to well-coated (solid black line, Fig. A1) particle size distribution curves, H_2SO_4 coating in this case results in particle number concentration losses and a small-sized growth.

Figure A2 shows the mass distribution of 200 nm bare and H_2SO_4-coated mCASTblack soot particles. The larger mass distribution-mode value of coated soot particles doubtlessly demonstrates the adsorption/condensation of H_2SO_4 on the soot aggregates. The mass distribution curve also provides evidence of the internal mixing state of soot particles with H_2SO_4, given that the curve only shows one single distinct peak with a log-normal fitting peak value at 1.93 fg. It is conceivable that there are no 200 nm pure H_2SO_4 particles in the aerosol flow because a 200 nm pure H_2SO_4 particle has a mass of 7.7 fg.

Because of the heterogeneity of soot particles and the poor assumption for its spherical structure, DMA cannot perfectly select monodisperse soot particles based on the electrical mobility diameter. Therefore, we measured the number size distribution of the size-selected bare soot particles using an SMPS system with multiple-charged particle correction, downstream of the DMA. The DMA and the SMPS system were operated with the same configurations as for all ice nucleation experiments. For 200 nm soot particles, the DMA was running with a sheath to aerosol flow ratio of 10 : 1 and the downstream SMPS system with a flow ratio of 4 : 1. The system was pulled by a CPC 3772 with a sample flow rate of 1 L min^{-1}. For 400 nm soot particles, the DMA sheath to aerosol flow ratio was 7 : 1, and the SMPS system operat-

ing with a CPC 3776 in low-flow mode (aerosol sample flow 0.3 L min^{-1}) had a sheath to aerosol flow ratio of 6 : 1. As shown in Figs. A3 and A4, SMPS measurements are able to cover the double-charged size for 200 and 400 nm soot particles, and there exists a significant proportion ($> 15\%$) of soot particles with larger sizes than the size selection value. It is likely that these double-charged particles of larger size than the size selection value first nucleate ice during the RH scan experiments, given the size dependence of soot ice nucleation.

Appendix B: The ice nucleation activity of bare and H_2SO_4-coated soot particles

Soot particles coated by H_2SO_4 with progressively increasing coating masses were systematically investigated for their ice nucleation activities. The coating thickness was from less than a complete H_2SO_4 monolayer coverage up to several equivalent monolayers. Figures B1 to B4 present the AF plots derived from 1 μm OPC channel data of all the soot samples investigated as a function of RH (RH_i and RH_w), and AF curves based on 5 μm OPC channel data are presented in Figs. B5 to B8. These figures show that at 243 and 238 K the signal in the 5 μm OPC channel at $RH_w < 105\%$ is absent, thus suggesting that no ice crystals form at these temperatures and that only water droplets are present in the 1 μm channel. This is because if ice can be nucleated at 243 and 238 K, the ice crystals grow sufficiently large to be reliably detected in the 5 μm channel for $RH_w < 105\%$ but water droplets do not. As such, we can confidently conclude no ice nucleation for our soot particles at $T = 243$ and 238 K. For both mCASTblack and FW200 soot, at least eight H_2SO_4 coating wt % were tested for size-selected soot particles of a size 200 or 400 nm.
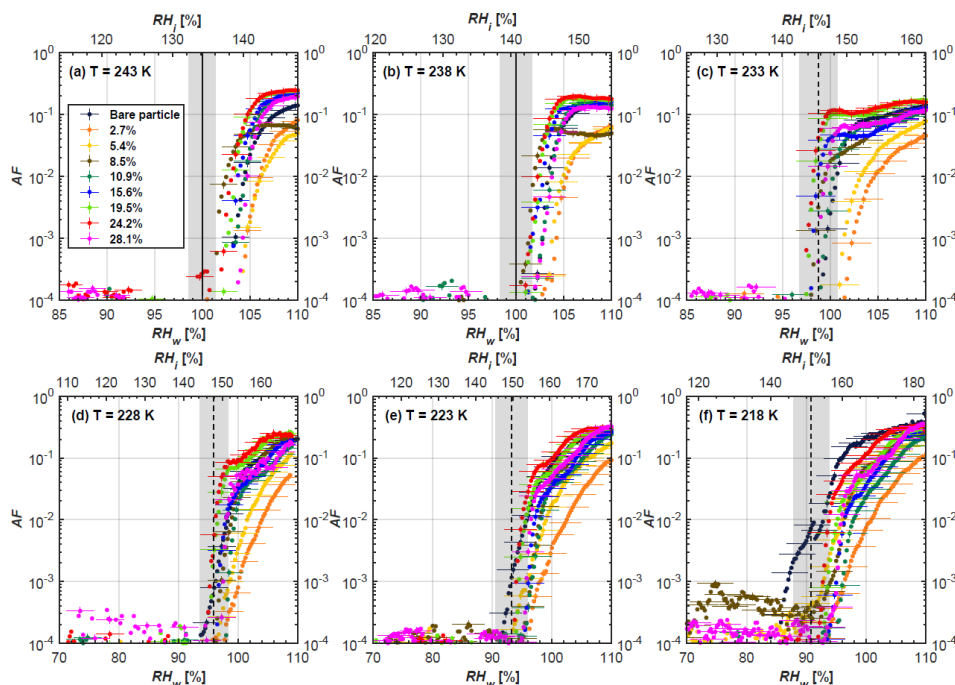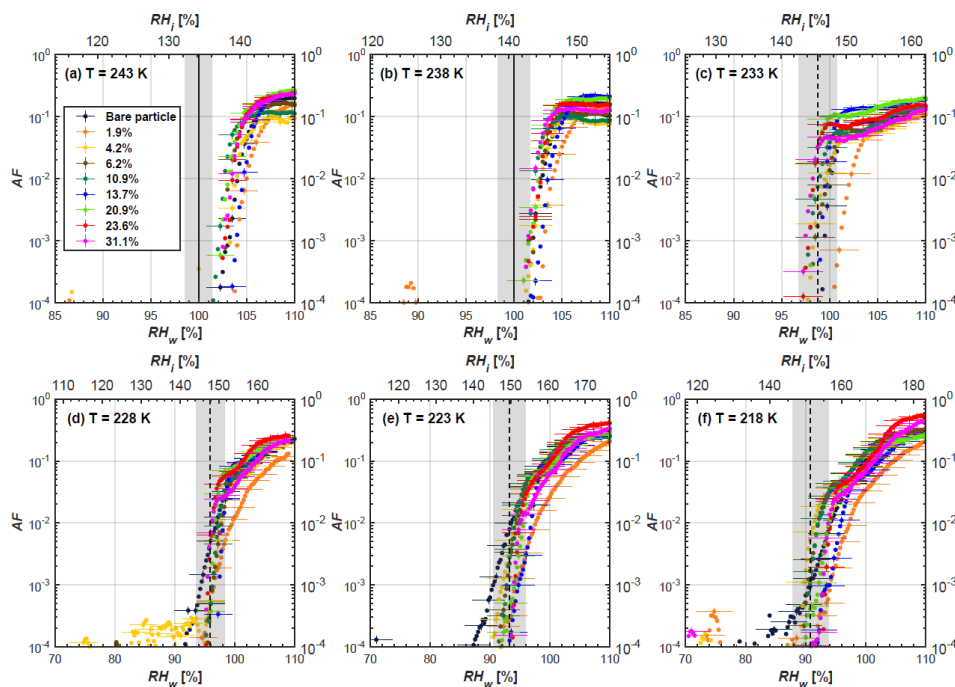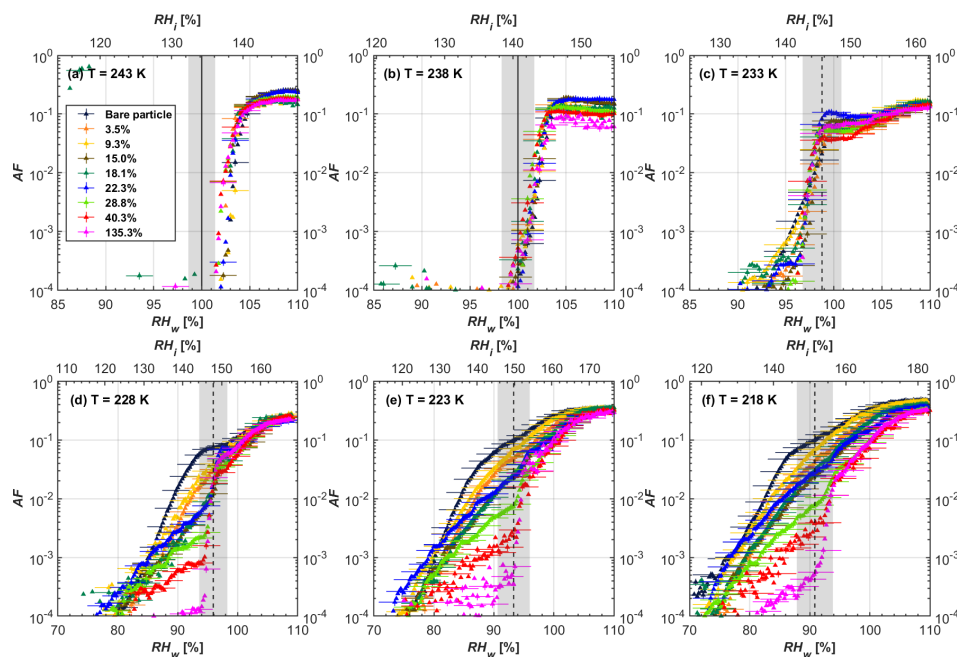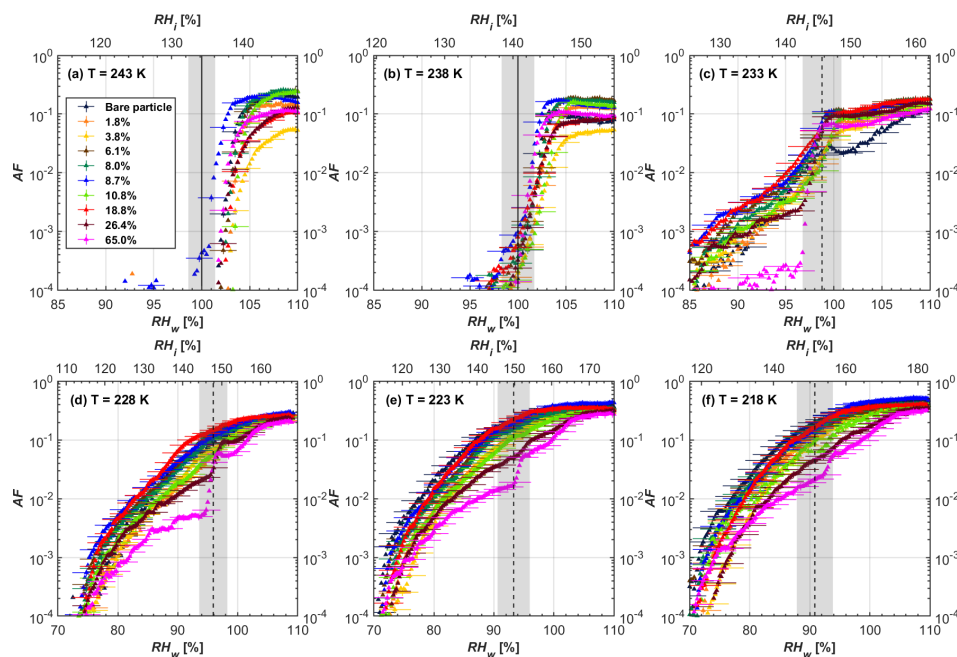
Figure B1. RH scans for bare and coated 200 nm mCASTblack soot particles at eight different coating wt % corresponding to the 1 μm OPC channel, presented as AF as a function of RH. Black solid lines represent water saturation conditions according to Murphy and Koop (2005). Black dashed lines denote the expected RH values for homogeneous freezing at $T < $ HNT (Koop et al., 2000). The grey-shaded areas show the possible RH uncertainty calculated for water saturation and homogeneous freezing conditions. The percentage number represents the H_2SO_4 coating mass ratio to the bare particle mass.
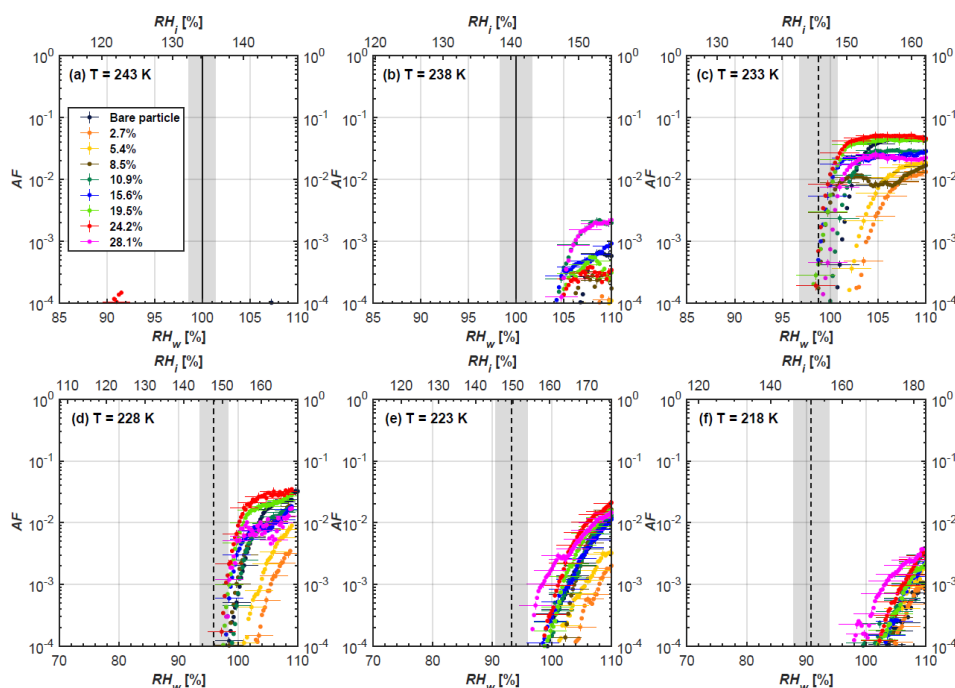

Figure B2. RH scans for bare and coated 400 nm mCASTblack soot particles at eight different coating wt % corresponding to the 1 μm OPC channel, presented as AF as a function of RH. Black solid lines represent water saturation conditions according to Murphy and Koop (2005). Black dashed lines denote the expected RH values for homogeneous freezing at $T < $ HNT (Koop et al., 2000). The grey-shaded areas show the possible RH uncertainty calculated for water saturation and homogeneous freezing conditions. The percentage number represents the H_2SO_4 coating mass ratio to the bare particle mass.
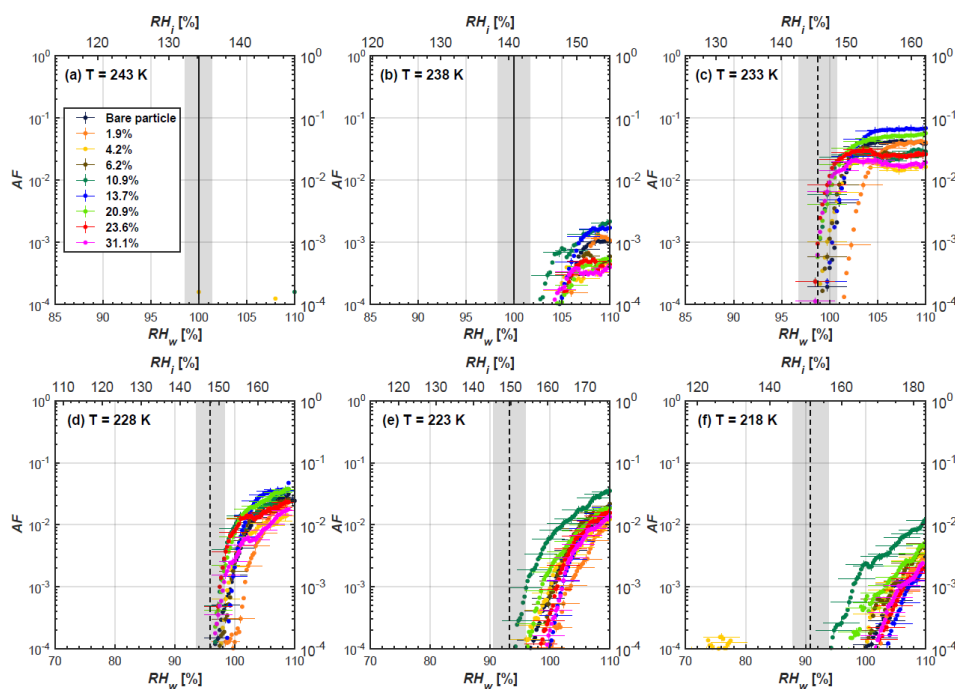
Figure B3. RH scans for bare and coated 200 nm FW200 soot particles at eight different coating wt % corresponding to the 1 μm OPC channel, presented as AF as a function of RH. Black solid lines represent water saturation conditions according to Murphy and Koop (2005). Black dashed lines denote the expected RH values for homogeneous freezing at $T <$ HNT (Koop et al., 2000). The grey-shaded areas show the possible RH uncertainty calculated for water saturation and homogeneous freezing conditions. The percentage number represents the H_2SO_4 coating mass ratio to the bare particle mass.
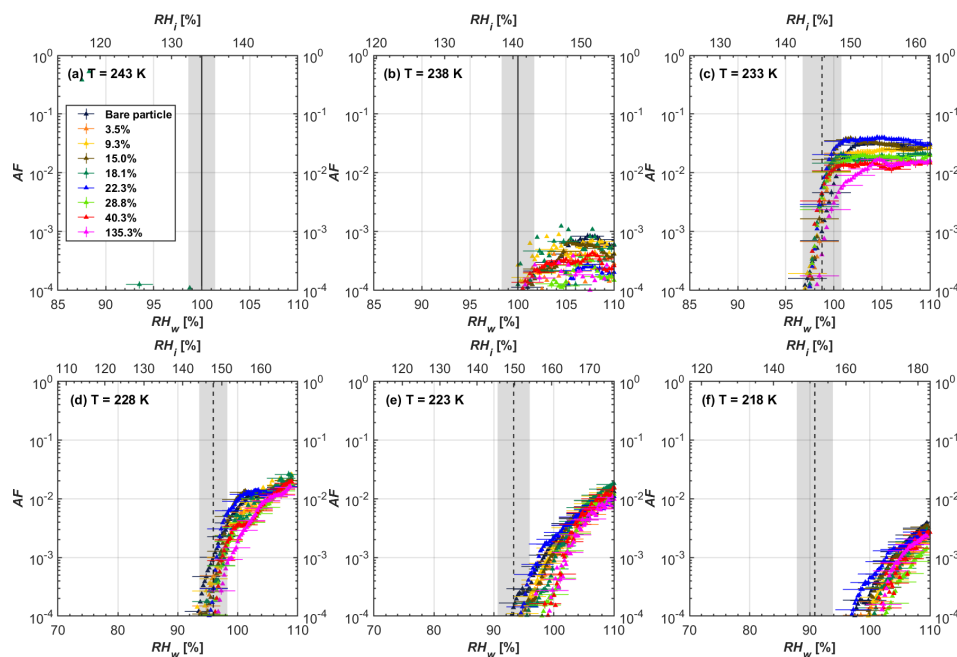

Figure B4. RH scans for bare and coated 400 nm FW200 soot particles at nine different coating wt % corresponding to the 1 μm OPC channel, presented as AF as a function of RH. Black solid lines represent water saturation conditions according to Murphy and Koop (2005). Black dashed lines denote the expected RH values for homogeneous freezing at $T <$ HNT (Koop et al., 2000). The grey-shaded areas show the possible RH uncertainty calculated for water saturation and homogeneous freezing conditions. The percentage number represents the H_2SO_4 coating mass ratio to the bare particle mass.
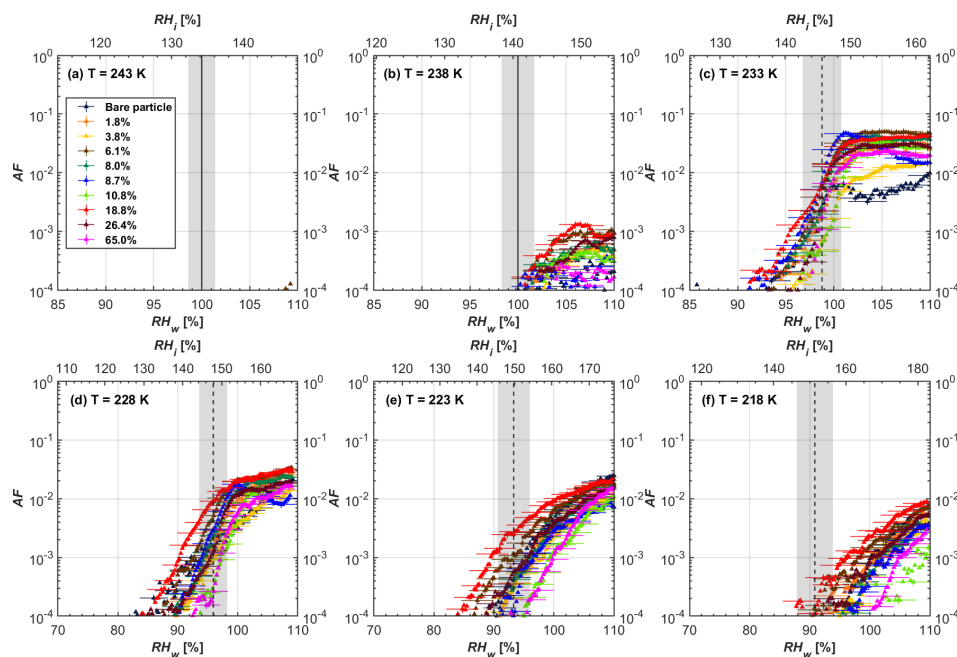
Figure B5. RH scans for bare and coated 200 nm mCASTblack soot particles at eight different coating wt % corresponding to the 5 µm OPC channel, presented as AF as a function of RH. Black solid lines represent water saturation conditions according to Murphy and Koop (2005). Black dashed lines denote the expected RH values for homogeneous freezing at $T <$ HNT (Koop et al., 2000). The grey-shaded areas show the possible RH uncertainty calculated for water saturation and homogeneous freezing conditions. The percentage number represents the H_2SO_4 coating mass ratio to the bare particle mass.

Figure B6. RH scans for bare and coated 400 nm mCASTblack soot particles at eight different coating wt % corresponding to the 5 µm OPC channel, presented as AF as a function of RH. Black solid lines represent water saturation conditions according to Murphy and Koop (2005). Black dashed lines denote the expected RH values for homogeneous freezing at $T <$ HNT (Koop et al., 2000). The grey-shaded areas show the possible RH uncertainty calculated for water saturation and homogeneous freezing conditions. The percentage number represents the H_2SO_4 coating mass ratio to the bare particle mass.

Figure B7. RH scans for bare and coated 200 nm FW200 soot particles at eight different coating wt % corresponding to the 5 μm OPC channel, presented as AF as a function of RH. Black solid lines represent water saturation conditions according to Murphy and Koop (2005). Black dashed lines denote the expected RH values for homogeneous freezing at $T < $ HNT (Koop et al., 2000). The grey-shaded areas show the possible RH uncertainty calculated for water saturation and homogeneous freezing conditions. The percentage number represents the H_2SO_4 coating mass ratio to the bare particle mass.

Figure B8. RH scans for bare and coated 400 nm FW200 soot particles at nine different coating wt % corresponding to the 5 μm OPC channel, presented as AF as a function of RH. Black solid lines represent water saturation conditions according to Murphy and Koop (2005). Black dashed lines denote the expected RH values for homogeneous freezing at $T < $ HNT (Koop et al., 2000). The grey-shaded areas show the possible RH uncertainty calculated for water saturation and homogeneous freezing conditions. The percentage number represents the H_2SO_4 coating mass ratio to the bare particle mass.

Appendix C: Supplementary SEM, TEM and EDX results to characterize particle morphology

SEM and TEM images taken from the same grid samples as for Figs. 8 and 9 but at low resolutions showing an overview of particle morphologies are presented in Fig. C1 (400 nm soot aggregates) and Fig. C2 (200 nm soot aggregates), respectively. The SEM images at 20 k magnification in Fig. C1 show that thickly coated soot particles, both for mCASTblack and FW200, are more compacted, whereas thinly coated particles are similar to the bare ones. The same findings can be supported by TEM images at low magnification values in Fig. C2. Additionally, some small residues, surrounding single soot aggregates in Fig. C2f, are believed to be the footprint of small H_2SO_4 droplets generated during the impaction and evaporation of these coated soot particles.

However, the visualized particles at low magnifications are larger than the particle sample's selected size. As explained in Sect. 3.3.1, the most probable reason is the soot-aggregate agglomeration during impaction onto the grid, particularly when the particle concentration is high. This can explain why mCASTblack soot aggregates in Fig. C1a, b and c are much larger than 400 nm, i.e. the size selection value. During TEM sample grid collection, the particle number concentration of 400 nm mCASTblack soot particles was as high as 3000 cm^{-3}, providing a high probability of these mCASTblack soot aggregates agglomerating into larger clusters (> 400 nm) when sampling onto the grid by impaction. In order to exclude other possible artifacts, the optical sizes of suspended 200 and 400 nm mCASTblack size-selected bare soot particle samples were measured by the OPC, operated in the same manner as for HINC experiments. The measurement aerosol flow, also with a particle number concentration ~ 3000 cm^{-3} measured by a low-flow mode CPC 3776 at a 0.3 L min^{-1} flow rate, was first sampled upstream of ZEMI. Then the sample concentration was diluted to lower than the coincidence limit of the OPC (~ 106 cm^{-3}). Each OPC channel logged the number of particles larger than the channel threshold value in a 5 s interval. After measuring for 5 min, the percentage of 200 and 400 nm mCASTblack bare soot particles in different OPC counting channels could be calculated. As shown in Fig. C3a, only 2.08 % of 200 nm size-selected mCASTblack soot particles are detected with an optical size larger than 0.3 µm, suggesting larger soot aggregates in Fig. 9a and b are agglomerates of 200 nm aggregates. Similarly, 400 nm size-selected mCASTblack soot aerosol only contains 0.04 % of particles larger than 1 µm optical size, whereas 99.96 % of the particles are of an optical size between 0.3 and 1 µm (see Fig. C3b). This further supports our claim that the supermicron-sized soot particles shown in Figs. C1 and C2 are agglomerates of small soot aggregates.

HR-TEM images are also collected to determine how the H_2SO_4 coating changes the fine structures of soot aggregates and the network among primary particles, i.e. soot spheres
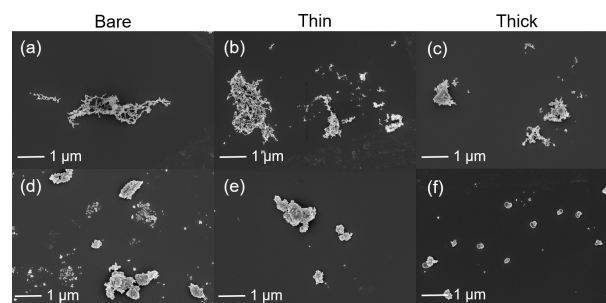

Figure C1. SEM images (Zeiss Leo 1530, Signal = InLens, EHT = 3 kV) for 400 nm size-selected bare and coated mCAST-black and FW200 soot particles. Scale bars are indicated in each image. **(a)** Bare mCASTblack, **(b)** mCASTblack with a thin coating (coating wt = 1.9 %), **(c)** mCASTblack with a thick coating (coating wt = 31.1 %), **(d)** bare FW200, **(e)** FW200 with a thin coating (coating wt = 1.8 %), and **(f)** FW200 with a thin coating (coating wt = 65.0 %).
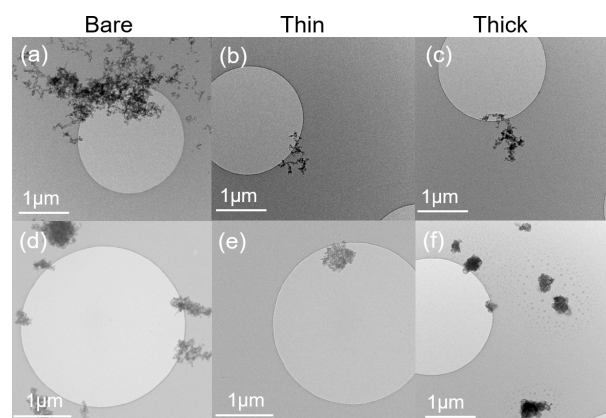

Figure C2. TEM images for 200 nm size-selected bare and coated mCASTblack and FW200 soot particles with a lower magnification as shown in each image. Scale bars are indicated in each image. **(a)** Bare mCASTblack, **(b)** mCASTblack with a thin coating (coating wt = 2.9 %), **(c)** mCASTblack with a thick coating (coating wt = 30.2 %), **(d)** bare FW200, **(e)** FW200 with a thin coating (coating wt = 2.3 %), and **(f)** FW200 with a thin coating (coating wt = 139.3 %). Microscopes used: **(a)**–**(c)** and **(f)** TFS F30, **(d)** and **(e)** Hitachi HT7700.

showing a distinct onion-like structure comprising graphitic layers in Fig. C4. In order to avoid the background noise from the carbon film on the Cu grid, soot aggregates hanging outside of the mesh edge (i.e. in the holes) were selected to obtain these HR-TEM images. The primary particle profiles in these 2D projected soot-aggregate images are still distinguishable in Fig. C4d for bare and Fig. C4e for thinly coated soot particles, but single primary particle edges are more ambiguous in Fig. C4f for thickly coated soot particles. The similar results can be seen from Fig. C5, in which the outline of FW200 soot primary particles with thick coating (Fig. C5f) is smoother than those of bare and thinly coated
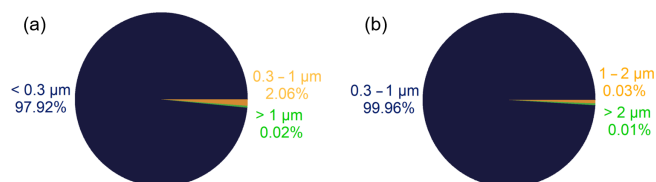
Figure C3. The percentage of 200 **(a)** and 400 nm **(b)** size-selected mCASTblack bare soot particles in three optical size ranges measured by the OPC operating in different counting channels, including 0.3, 1 and 2 μm.
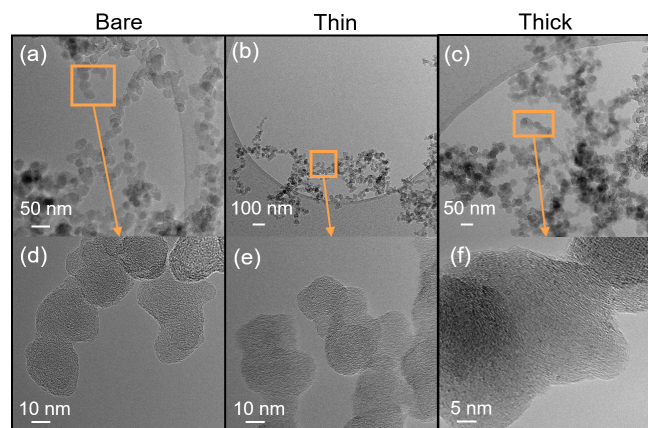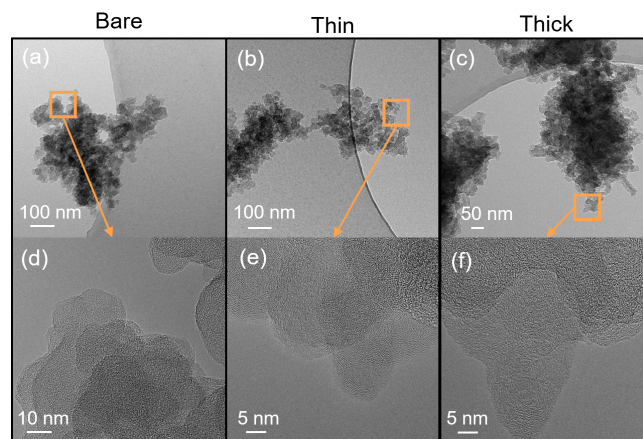

Figure C4. HR-TEM images for fine structures of 200 nm size-selected bare and coated mCASTblack soot particles. Scale bars are indicated in each image. **(a, d)** Bare particles, **(b, e)** thinly coated particles with a coating wt = 2.9 %, and **(c, f)** thickly coated particles with a coating wt = 30.2 %. All images taken with TFS F30.

Figure C5. HR-TEM images for fine structures of 200 nm size-selected bare and coated FW200 soot particles. Scale bars are indicated in each image. **(a, d)** Bare particles, **(b, e)** thinly coated particles with a coating wt = 2.3 %, and **(c, f)** thickly coated particles with a coating wt = 139.3 %. All images taken with TFS F30.

As shown in Figs. 10 and 11, C, O and S normalized mass percentages in the areas of interest (AOI) on the soot-aggregate surface are presented. These results are calculated from the EDX spectra shown below in Figs. C6 to C11. The three peaks, at 0.93 (copper, $K\alpha$), 1.74 (silicon, $K\alpha$) and 8.10 eV (copper, $L\alpha$), are from the microscopy grid material and are not included in the analysis.
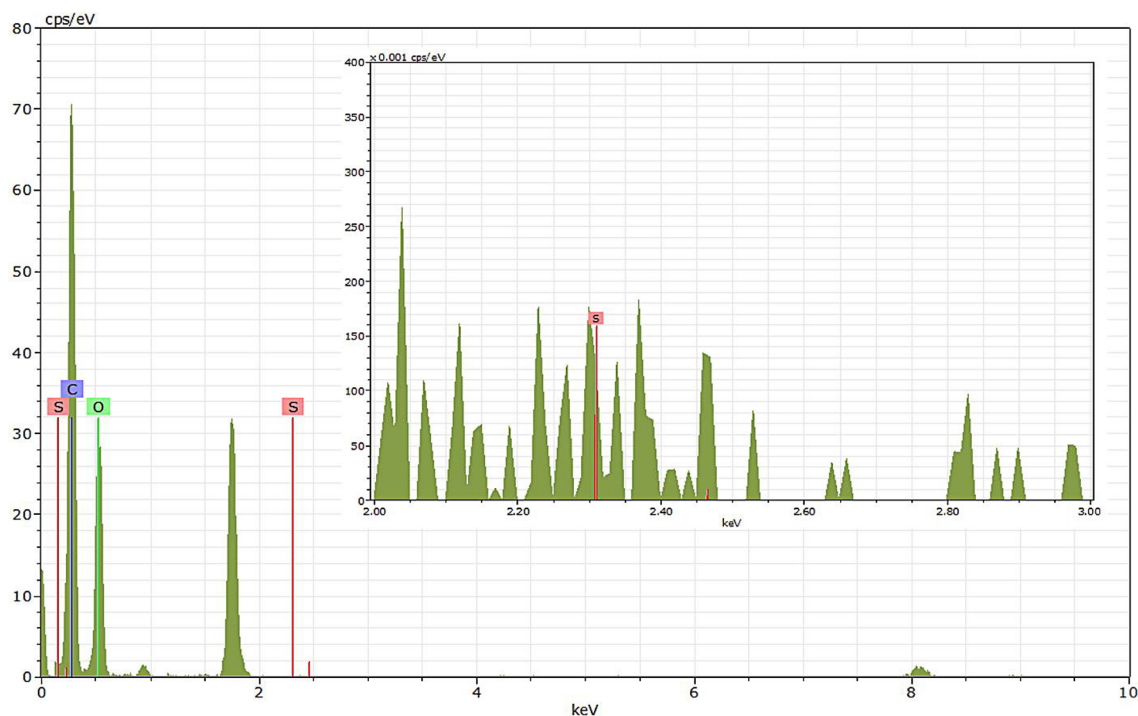
particles (Fig. C5d and e). This can be attributed to the pore-filling effect of H_2SO_4 coating, which fills in voids or wedges among primary particles and reduces the roughness of the soot-aggregate surface.

Figure C6. Energy-dispersive X-ray spectroscopy (EDX) spectra for AOI of bare mCASTblack soot presented in Fig. 10. The x axis stands for the electron energy (keV) and the y axis represents counts per second per eV (cps eV^{-1}). The position of carbon (C), oxygen (O) and sulfur (S) is indicated in the figure. The zoom-in patch shows the sulfur region of the spectra, which is not legible in the main spectrum.
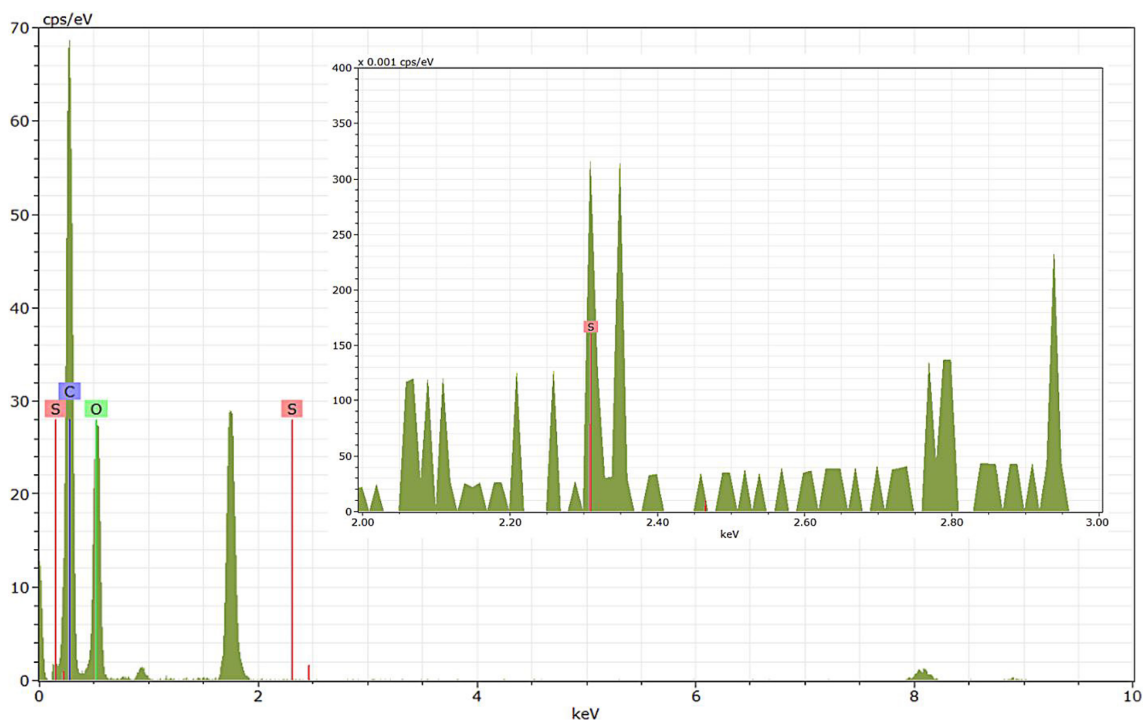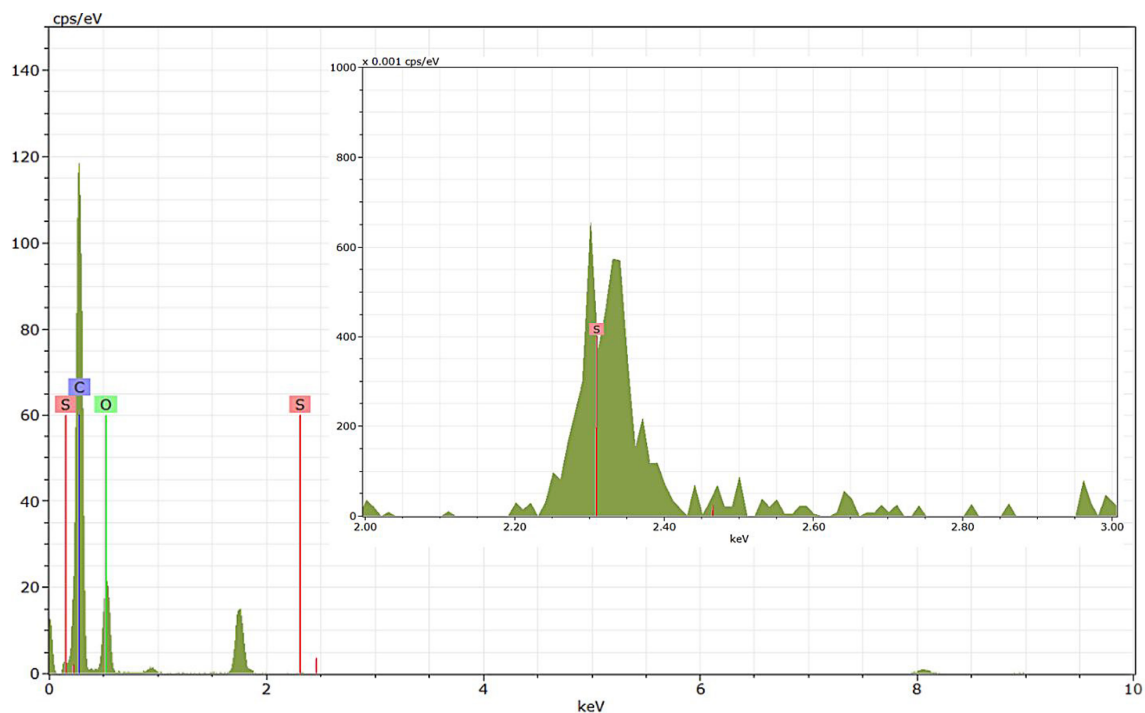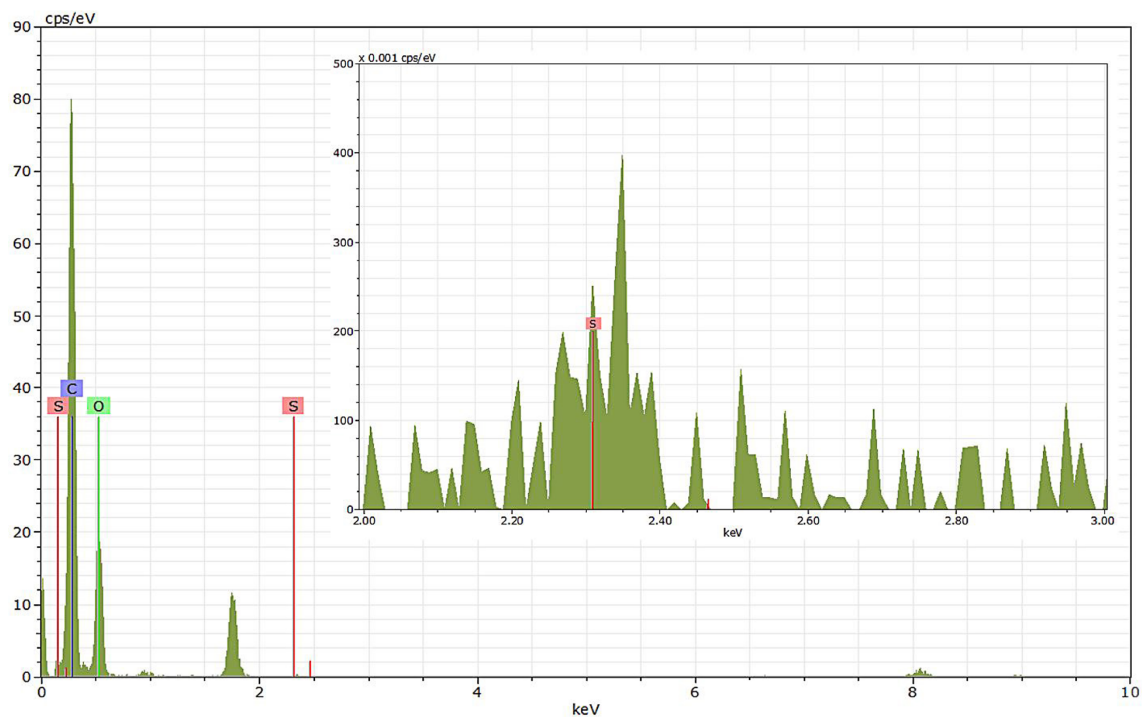

Figure C7. EDX spectra for AOI of thinly coated mCASTblack soot (H$_2$SO$_4$ coating wt $= 2.9$ %) presented in Fig. 10. The x axis stands for the electron energy (keV) and the y axis represents counts per second per eV (cps eV^{-1}). The position of carbon (C), oxygen (O) and sulfur (S) is indicated in the figure. The zoom-in patch shows the sulfur region of the spectra, which is not legible in the main spectrum.
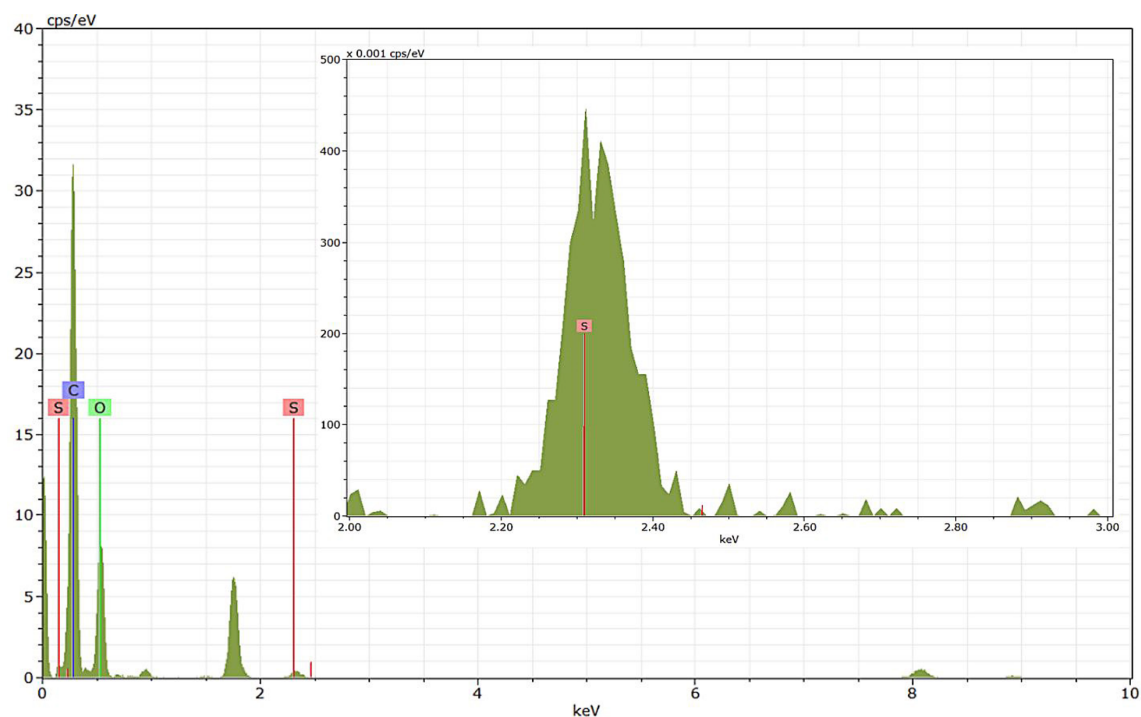
Figure C8. EDX spectra for AOI of thickly coated mCASTblack soot (H_2SO_4 coating wt $= 30.2\%$) presented in Fig. 10. The x axis stands for the electron energy (keV) and the y axis represents counts per second per eV (cps eV^{-1}). The position of carbon (C), oxygen (O) and sulfur (S) is indicated in the figure. The zoom-in patch shows the sulfur region of the spectra, which is not legible in the main spectrum.

Figure C9. EDX spectra for AOI of bare FW200 soot presented in Fig. 11. The x axis stands for the electron energy (keV) and the y axis represents counts per second per eV (cps eV^{-1}). The position of carbon (C), oxygen (O) and sulfur (S) is indicated in the figure. The zoom-in patch shows the sulfur region of the spectra, which is not legible in the main spectrum.
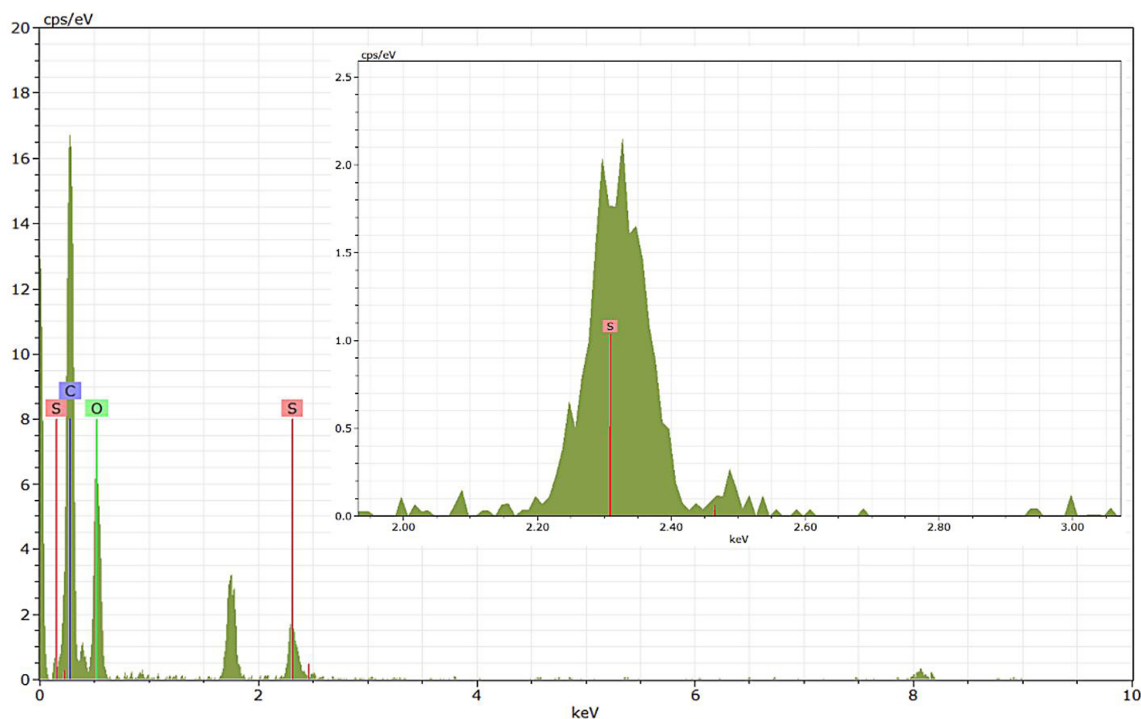
Figure C10. EDX spectra for AOI of thinly coated FW200 soot (H_2SO_4 coating wt $= 2.3$ %) presented in Fig. 11. The x axis stands for the electron energy (keV) and the y axis represents counts per second per eV (cps eV^{-1}). The position of carbon (C), oxygen (O) and sulfur (S) is indicated in the figure. The zoom-in patch shows the sulfur region of the spectra, which is not legible in the main spectrum.

Figure C11. EDX spectra for AOI of thickly coated FW200 soot (H_2SO_4 coating wt $= 139.3$ %) presented in Fig. 11. The x axis stands for the electron energy (keV) and the y axis represents counts per second per eV (cps eV^{-1}). The position of carbon (C), oxygen (O) and sulfur (S) is indicated in the figure. The zoom-in patch shows the sulfur region of the spectra, which is not legible in the main spectrum.

References

Adachi, K., Freney, E. J., and Buseck, P. R.: Shapes of internally mixed hygroscopic aerosol particles after deliquescence, and their effect on light scattering, Geophys. Res. Lett., 38, L13804, https://doi.org/10.1029/2011gl047540, 2011.

Bambha, R. P., Dansson, M. A., Schrader, P. E., and Michelsen, H. A.: Effects of Volatile Coatings on the Morphology and Optical Detection of Combustion-Generated Black Carbon Particles, Remote Sensing and Combustion Chemistry Departments Sandia National Laboratories, https://doi.org/10.2172/1096459, 2013.

Bhandari, J., China, S., Chandrakar, K. K., Kinney, G., Cantrell, W., Shaw, R. A., Mazzoleni, L. R., Girotto, G., Sharma, N., Gorkowski, K., Gilardoni, S., Decesari, S., Facchini, M. C., Zanca, N., Pavese, G., Esposito, F., Dubey, M. K., Aiken, A. C., Chakrabarty, R. K., Moosmuller, H., Onasch, T. B., Zaveri, R. A., Scarnato, B. V., Fialho, P., and Mazzoleni, C.: Extensive Soot Compaction by Cloud Processing from Laboratory and Field Ob-

servations, Sci. Rep., 9, 11824, https://doi.org/10.1038/s41598-019-48143-y, 2019.

Biggs, C. I., Packer, C., Hindmarsh, S., Walker, M., Wilson, N. R., Rourke, J. P., and Gibson, M. I.: Impact of sequential surface-modification of graphene oxide on ice nucleation, Phys. Chem. Chem. Phys., 19, 21929–21932, https://doi.org/10.1039/c7cp03219f, 2017.

Bond, T. C., Doherty, S. J., Fahey, D. W., Forster, P. M., Berntsen, T., DeAngelo, B. J., Flanner, M. G., Ghan, S., Kärcher, B., Koch, D., Kinne, S., Kondo, Y., Quinn, P. K., Sarofim, M. C., Schultz, M. G., Schulz, M., Venkataraman, C., Zhang, H., Zhang, S., Bellouin, N., Guttikunda, S. K., Hopke, P. K., Jacobson, M. Z., Kaiser, J. W., Klimont, Z., Lohmann, U., Schwarz, J. P., Shindell, D., Storelvmo, T., Warren, S. G., and Zender, C. S.: Bounding the role of black carbon in the climate system: A scientific assessment, J. Phys. Chem. A, 118, 5380–5552, https://doi.org/10.1002/jgrd.50171, 2013.

Braun-Unkhoff, M., Riedel, U., and Wahl, C.: About the emissions of alternative jet fuels, CEAS Aeronaut. J., 8, 167–180, https://doi.org/10.1007/s13272-016-0230-3, 2016.

Brito, J., Rizzo, L. V., Morgan, W. T., Coe, H., Johnson, B., Haywood, J., Longo, K., Freitas, S., Andreae, M. O., and Artaxo, P.: Ground-based aerosol characterization during the South American Biomass Burning Analysis (SAMBBA) field experiment, Atmos. Chem. Phys., 14, 12069–12083, https://doi.org/10.5194/acp-14-12069-2014, 2014.

Brown, A. P.: Contrail Flight Data for a Variety of Jet Fuels, 2018 Atmos. Space Environ. Conf., AIAA 2018-3188, https://doi.org/10.2514/6.2018-3188, 2018.

Brunauer, S., Emmett, P. J., and Teller, E.: Absorption of gasses in multimolecular layers, J. Am. Chem. Soc., 60, 309–319, 1938.

Chen, Y., Kreidenweis, S. M., McInnes, L. M., Rogers, D. C., and DeMott, P. J.: Single particle analyses of ice-nucleating aerosols in the upper troposphere and lower stratosphere, Geophys. Res. Lett., 25, 1391–1394, 1998.

China, S., Scarnato, B., Owen, R. C., Zhang, B., Ampadu, M. T., Kumar, S., Dzepina, K., Dziobak, M. P., Fialho, P., Perlinger, J. A., Hueber, J., Helmig, D., Mazzoleni, L. R., and Mazzoleni, C.: Morphology and mixing state of aged soot particles at a remote marine free troposphere site: Implications for optical properties, Geophys. Res. Lett., 42, 1243–1250, https://doi.org/10.1002/2014gl062404, 2015.

Colbeck, I., Appleby, L., Hardman, E. J., and Harrison, R. M.: The optical properties and morphology of cloud-processed carbonaceous smoke, J. Aerosol Sci., 21, 527–538, https://doi.org/10.1016/0021-8502(90)90129-L, 1990.

Crawford, I., Möhler, O., Schnaiter, M., Saathoff, H., Liu, D., McMeeking, G., Linke, C., Flynn, M., Bower, K. N., Connolly, P. J., Gallagher, M. W., and Coe, H.: Studies of propane flame soot acting as heterogeneous ice nuclei in conjunction with single particle soot photometer measurements, Atmos. Chem. Phys., 11, 9549–9561, https://doi.org/10.5194/acp-11-9549-2011, 2011.

Curtius, J.: Sulfuric acid measurements in the exhaust plume of a jet aircraft in flight: Implications for the sulfuric acid formation efficiency, Geophys Res. Lett., 29, 1113, https://doi.org/10.1029/2001gl013813, 2002.

Cziczo, D. J. and Froyd, K. D.: Sampling the composition of cirrus ice residuals, Atmos. Res., 142, 15–31, https://doi.org/10.1016/j.atmosres.2013.06.012, 2014.

Cziczo, D. J., Froyd, K. D., Hoose, C., Jensen, E. J., Diao, M., Zondlo, M. A., Smith, J. B., Twohy, C. H., and Murphy, D. M.: Clarifying the Dominant Sources and Mechanisms of Cirrus Cloud Formation, Science, 340, 1320–1324, 2013.

Dalirian, M., Ylisirniö, A., Buchholz, A., Schlesinger, D., Ström, J., Virtanen, A., and Riipinen, I.: Cloud droplet activation of black carbon particles coated with organic compounds of varying solubility, Atmos. Chem. Phys., 18, 12477–12489, https://doi.org/10.5194/acp-18-12477-2018, 2018.

David, R. O., Fahrni, J., Marcolli, C., Mahrt, F., Brühwiler, D., and Kanji, Z. A.: The role of contact angle and pore width on pore condensation and freezing, Atmos. Chem. Phys., 20, 9419–9440, https://doi.org/10.5194/acp-20-9419-2020, 2020.

DeMott, P. J., Chen, Y., Kreidenweis, S. M., Rogers, D. C., and Sherman, D. E.: Ice formation by black carbon particles, Geophys. Res. Lett., 26, 2429–2432, https://doi.org/10.1029/1999gl900580, 1999.

Ditas, J., Ma, N., Zhang, Y., Assmann, D., Neumaier, M., Riede, H., Karu, E., Williams, J., Scharffe, D., Wang, Q., Saturno, J., Schwarz, J. P., Katich, J. M., McMeeking, G. R., Zahn, A., Hermann, M., Brenninkmeijer, C. A. M., Andreae, M. O., Poschl, U., Su, H., and Cheng, Y.: Strong impact of wildfires on the abundance and aging of black carbon in the lowermost stratosphere, P. Natl. Acad. Sci. USA, 115, E11595–E11603, https://doi.org/10.1073/pnas.1806868115, 2018.

Ess, M. N. and Vasilatou, K.: Characterization of a new mini-CAST with diffusion flame and premixed flame options: Generation of particles with high EC content in the size range 30 nm to 200 nm, Aerosol Sci. Tech., 53, 29–44, https://doi.org/10.1080/02786826.2018.1536818, 2018.

Friedman, B., Kulkarni, G., Beránek, J., Zelenyuk, A., Thornton, J. A., and Cziczo, D. J.: Ice nucleation and droplet formation by bare and coated soot particles, J. Geophys. Res., 116, D17203, https://doi.org/10.1029/2011jd015999, 2011.

Fushimi, A., Saitoh, K., Fujitani, Y., and Takegawa, N.: Identification of jet lubrication oil as a major component of aircraft exhaust nanoparticles, Atmos. Chem. Phys., 19, 6389–6399, https://doi.org/10.5194/acp-19-6389-2019, 2019.

Gao, K., Friebel, F., Zhou, C.-W., and Kanji, Z. A.: Enhanced soot particle ice nucleation ability induced by aggregate compaction and densification, Atmos. Chem. Phys., 22, 4985–5016, https://doi.org/10.5194/acp-22-4985-2022, 2022a.

Gao, K., Zhou, C.-W., Barthazy, M. E., and Kanji, Z. A.: Ice nucleation activities of soot particles internally mixed with sulfuric acid at cirrus cloud conditions, ETH Zurich [data set], https://doi.org/10.3929/ethz-b-000498786, 2022b.

Garland, E. R., Rosen, E. P., Clarke, L. I., and Baer, T.: Structure of submonolayer oleic acid coverages on inorganic aerosol particles: evidence of island formation, Phys. Chem. Chem. Phys., 10, 3156–3161, https://doi.org/10.1039/b718013f, 2008.

Hallett, J., Hudson, J. G., and Rogers, C. F.: Characterization of Combustion Aerosols for Haze and Cloud Formation, Aerosol Sci. Tech., 10, 70–83, https://doi.org/10.1080/02786828908959222, 1989.

Hausler, T., Gebhardt, P., Iglesias, D., Rameshan, C., Marchesan, S., Eder, D., and Grothe, H.: Ice Nucleation Activity of Graphene and Graphene Oxides, J. Phys. Chem. C, 122, 8182–8190, https://doi.org/10.1021/acs.jpcc.7b10675, 2018.

Henson, B. F.: An adsorption model of insoluble particle activation: Application to black carbon, J. Geophys. Res., 112, D24S16, https://doi.org/10.1029/2007jd008549, 2007.

Hu, D., Liu, D., Kong, S., Zhao, D., Wu, Y., Li, S., Ding, S., Zheng, S., Cheng, Y., Hu, K., Deng, Z., Wu, Y., Tian, P., Liu, Q., Huang, M., and Ding, D.: Direct Quantification of Droplet Activation of Ambient Black Carbon Under Water Supersaturation, J. Geophys. Res.-Atmos., 126, e2021JD034649, https://doi.org/10.1029/2021jd034649, 2021.

Kanji, Z. A. and Abbatt, J. P. D.: The University of Toronto Continuous Flow Diffusion Chamber (UT-CFDC): A Simple Design for Ice Nucleation Studies, Aerosol Sci. Tech., 43, 730–738, https://doi.org/10.1080/02786820902889861, 2009.

Kanji, Z. A., DeMott, P. J., Möhler, O., and Abbatt, J. P. D.: Results from the University of Toronto continuous flow diffusion chamber at ICIS 2007: instrument intercomparison and ice onsets for different aerosol types, Atmos. Chem. Phys., 11, 31–41, https://doi.org/10.5194/acp-11-31-2011, 2011.

Kanji, Z. A., Ladino, L. A., Wex, H., Boose, Y., Burkert-Kohn, M., Cziczo, D. J., and Krämer, M.: Chapter 1 Overview of Ice Nucleating Particles, Meteorol. Monogr., 58, 1.1–1.33, https://doi.org/10.1175/amsmonographs-d-16-0006.1, 2017.

Kanji, Z. A., Welti, A., Corbin, J. C., and Mensah, A. A.: Black Carbon Particles Do Not Matter for Immersion Mode Ice Nucleation, Geophys. Res. Lett., 47, e2019GL086764, https://doi.org/10.1029/2019gl086764, 2020.

Kärcher, B. and Lohmann, U.: A Parameterization of cirrus cloud formation: Homogeneous freezing including effects of aerosol size, J. Geophys. Res. Atmos., 107, AAC 9-1–AAC 9-10, https://doi.org/10.1029/2001jd001429, 2002.

Kärcher, B. and Yu, F.: Role of aircraft soot emissions in contrail formation, Geophys Res. Lett., 36, L01804, https://doi.org/10.1029/2008gl036649, 2009.

Kärcher, B., Kleine, J., Sauer, D., and Voigt, C.: Contrail Formation: Analysis of Sublimation Mechanisms, Geophys. Res. Lett., 45, 13547–13552, https://doi.org/10.1029/2018gl079391, 2018.

Kärcher, B., Mahrt, F., and Marcolli, C.: Process-oriented analysis of aircraft soot-cirrus interactions constrains the climate impact of aviation, Commun. Earth Environ., 2, 113, https://doi.org/10.1038/s43247-021-00175-x, 2021.

Khalizov, A. F., Zhang, R., Zhang, D., Xue, H., Pagels, J., and McMurry, P. H.: Formation of highly hygroscopic soot aerosols upon internal mixing with sulfuric acid vapor, J. Geophys. Res., 114, D05208, https://doi.org/10.1029/2008jd010595, 2009.

Kleine, J., Voigt, C., Sauer, D., Schlager, H., Scheibe, M., Jurkat-Witschas, T., Kaufmann, S., Kärcher, B., and Anderson, B. E.: In Situ Observations of Ice Particle Losses in a Young Persistent Contrail, Geophys. Res. Lett., 45, 13553–13561, https://doi.org/10.1029/2018gl079390, 2018.

Koehler, K. A., DeMott, P. J., Kreidenweis, S. M., Popovicheva, O. B., Petters, M. D., Carrico, C. M., Kireeva, E. D., Khokhlova, T. D., and Shonija, N. K.: Cloud condensation nuclei and ice nucleation activity of hydrophobic and hydrophilic soot particles, Phys. Chem. Chem. Phys., 11, 7759, https://doi.org/10.1039/b916865f, 2009.

Koop, T., Luo, B., Tsias, A., and Peter, T.: Water activity as the determinant for homogeneous ice nucleation in aqueous solutions, Nature, 406, 611–614, https://doi.org/10.1038/35020537, 2000.

Kulkarni, G., China, S., Liu, S., Nandasiri, M., Sharma, N., Wilson, J., Aiken, A. C., Chand, D., Laskin, A., Mazzoleni, C., Pekour, M., Shilling, J., Shutthanandan, V., Zelenyuk, A., and Zaveri, R. A.: Ice nucleation activity of diesel soot particles at cirrus relevant temperature conditions: Effects of hydration, secondary organics coating, soot morphology, and coagulation, Geophys. Res. Lett., 43, 3580–3588, https://doi.org/10.1002/2016gl068707, 2016.

Kulkarni, P., Baron, P. A., and Willeke, K.: Aerosol Measurement Principles, Techniques, and Applications, John Wiley & Sons, Inc., Hoboken, New Jersey, ISBN 978-0-470-38741-2, 2011.

Lacher, L., Lohmann, U., Boose, Y., Zipori, A., Herrmann, E., Bukowiecki, N., Steinbacher, M., and Kanji, Z. A.: The Horizontal Ice Nucleation Chamber (HINC): INP measurements at conditions relevant for mixed-phase clouds at the High Altitude Research Station Jungfraujoch, Atmos. Chem. Phys., 17, 15199–15224, https://doi.org/10.5194/acp-17-15199-2017, 2017.

Lee, D. S., Fahey, D. W., Skowron, A., Allen, M. R., Burkhardt, U., Chen, Q., Doherty, S. J., Freeman, S., Forster, P. M., Fuglestvedt, J., Gettelman, A., De Leon, R. R., Lim, L. L., Lund, M. T., Millar, R. J., Owen, B., Penner, J. E., Pitari, G., Prather, M. J., Sausen, R., and Wilcox, L. J.: The contribution of global aviation to anthropogenic climate forcing for 2000 to 2018, Atmos. Environ., 244, 117834, https://doi.org/10.1016/j.atmosenv.2020.117834, 2020.

Lee, D. S., Fahey, D. W., Skowron, A., Allen, M. R., Burkhardt, U., Chen, Q., Doherty, S. J., Freeman, S., Forster, P. M., Fuglestvedt, J., Gettelman, A., De Leon, R. R., Lim, L. L., Lund, M. T., Millar, R. J., Owen, B., Penner, J. E., Pitari, G., Prather, M. J., Sausen, R., and Wilcox, L. J.: The contribution of global aviation to anthropogenic climate forcing for 2000 to 2018, Atmos. Environ., 244, 117834, https://doi.org/10.1016/j.atmosenv.2020.117834, 2021.

Liou, K.-N.: Influence of cirrus clouds on weather and climate processes: A global perspective, Mon. Weather Rev., 114, 1167–1199, 1986.

Liu, D., He, C., Schwarz, J. P., and Wang, X.: Lifecycle of light-absorbing carbonaceous aerosols in the atmosphere, NPJ Clim. Atmos. Sci., 3, 40, https://doi.org/10.1038/s41612-020-00145-8, 2020.

Liu, J.: Estimating the average time for inter-continental transport of air pollutants, Geophys. Res. Lett., 32, L11814, https://doi.org/10.1029/2005gl022619, 2005.

Lohmann, U., LÜÖnd, F., and Mahrt, F.: An Introduction to Clouds From the Microscale to Climate, Cambridge University Press, 380 pp., ISBN 978-1-107-01822-8, 2016.

Lohmann, U., Friebel, F., Kanji, Z. A., Mahrt, F., Mensah, A. A., and Neubauer, D.: Future warming exacerbated by aged-soot effect on cloud formation, Nat. Geosci., 13, 674–680, https://doi.org/10.1038/s41561-020-0631-0, 2020.

Lowell, S., Shields, J. E., Thomas, M. A., and Thommes, M.: Characterization of Porous Solids and Powders: Surface Area, Pore Size and Density, Particle Technology Series, Kluwer Academic Publishers, Dordrecht, the Netherlands, https://doi.org/10.1007/978-1-4020-2303-3, 2004.

Lund, M. T., Samset, B. H., Skeie, R. B., Watson-Parris, D., Katich, J. M., Schwarz, J. P., and Weinzierl, B.: Short Black Carbon lifetime inferred from a global set of aircraft observations, NPJ Clim.

Atmos. Sci., 1, 31, https://doi.org/10.1038/s41612-018-0040-x, 2018.

Mahrt, F., Marcolli, C., David, R. O., Grönquist, P., Barthazy, M. E. J., Lohmann, U., and Kanji, Z. A.: Ice nucleation abilities of soot particles determined with the Horizontal Ice Nucleation Chamber, Atmos. Chem. Phys., 18, 13363–13392, https://doi.org/10.5194/acp-18-13363-2018, 2018.

Mahrt, F., Alpert, P. A., Dou, J., Gronquist, P., Arroyo, P. C., Ammann, M., Lohmann, U., and Kanji, Z. A.: Aging induced changes in ice nucleation activity of combustion aerosol as determined by near edge X-ray absorption fine structure (NEXAFS) spectroscopy, Environ. Sci.: Processes Impacts, 22, 895–907, https://doi.org/10.1039/c9em00525k, 2020a.

Mahrt, F., Kilchhofer, K., Marcolli, C., Grönquist, P., David, R. O., Rösch, M., Lohmann, U., and Kanji, Z. A.: The Impact of Cloud Processing on the Ice Nucleation Abilities of Soot Particles at Cirrus Temperatures, J. Geophys. Res.-Atmos., 125, 1–23, https://doi.org/10.1029/2019jd030922, 2020b.

Marcolli, C.: Deposition nucleation viewed as homogeneous or immersion freezing in pores and cavities, Atmos. Chem. Phys., 14, 2071–2104, https://doi.org/10.5194/acp-14-2071-2014, 2014.

Marcolli, C.: Pre-activation of aerosol particles by ice preserved in pores, Atmos. Chem. Phys., 17, 1595–1622, https://doi.org/10.5194/acp-17-1595-2017, 2017.

Marcolli, C.: Technical note: Fundamental aspects of ice nucleation via pore condensation and freezing including Laplace pressure and growth into macroscopic ice, Atmos. Chem. Phys., 20, 3209–3230, https://doi.org/10.5194/acp-20-3209-2020, 2020.

Marcolli, C., Mahrt, F., and Kärcher, B.: Soot PCF: pore condensation and freezing framework for soot aggregates, Atmos. Chem. Phys., 21, 7791–7843, https://doi.org/10.5194/acp-21-7791-2021, 2021.

Marhaba, I., Ferry, D., Laffon, C., Regier, T. Z., Ouf, F.-X., and Parent, P.: Aircraft and MiniCAST soot at the nanoscale, Combust. Flame, 204, 278–289, https://doi.org/10.1016/j.combustflame.2019.03.018, 2019.

McGraw, Z., Storelvmo, T., Samset, B. H., and Stjern, C. W.: Global Radiative Impacts of Black Carbon Acting as Ice Nucleating Particles, Geophys. Res. Lett., 47, e2020GL089056, https://doi.org/10.1029/2020gl089056, 2020.

McMurry, P. H., Wang, X., Park, K., and Ehara, K.: The Relationship between Mass and Mobility for Atmospheric Particles: A New Technique for Measuring Particle Density, Aerosol Sci. Tech., 36, 227–238, https://doi.org/10.1080/027868202753504083, 2002.

Möhler, O., Linke, C., Saathoff, H., Schnaiter, M., Wagner, R., Mangold, A., Krämer, M., and Schurath, U.: Ice nucleation on flame soot aerosol of different organic carbon content, Meteorol. Z., 14, 477–484, https://doi.org/10.1127/0941-2948/2005/0055, 2005a.

Möhler, O., Buttner, S., Linke, C., Schnaiter, M., Saathoff, H., Stetzer, O., Wagner, R., Kramer, M., Mangold, A., Ebert, V., and Schurath, U.: Effect of sulfuric acid coating on heterogeneous ice nucleation by soot aerosol particles, J. Geophys. Res., 110, D11210, https://doi.org/10.1029/2004jd005169, 2005b.

Motos, G., Corbin, J. C., Schmale, J., Modini, R. L., Bertò, M., Kupiszewski, P., Baltensperger, U., and Gysel-Beer, M.: Black Carbon Aerosols in the Lower Free Troposphere are Heavily Coated in Summer but Largely Uncoated in Winter

at Jungfraujoch in the Swiss Alps, Geophys. Res. Lett., 47, e2020GL088011, https://doi.org/10.1029/2020gl088011, 2020.

Muller, E. A., Rull, L. F., Vega, L. F., and Gubbins, K. E.: Adsorption of Water on Activated Carbons: A Molecular Simulation Study, J. Phys. Chem., 100, 1189–1196, https://doi.org/10.1021/jp952233w, 1996.

Murphy, D. M. and Koop, T.: Review of the vapour pressures of ice and supercooled water for atmospheric applications, Q. J. R. Meteorol. Soc., 131, 1539–1565, https://doi.org/10.1256/qj.04.94, 2005.

Nichman, L., Wolf, M., Davidovits, P., Onasch, T. B., Zhang, Y., Worsnop, D. R., Bhandari, J., Mazzoleni, C., and Cziczo, D. J.: Laboratory study of the heterogeneous ice nucleation on black-carbon-containing aerosol, Atmos. Chem. Phys., 19, 12175–12194, https://doi.org/10.5194/acp-19-12175-2019, 2019.

Okada, K., Ikegami, M., Zaizen, Y., Tsutsumi, Y., Makino, Y., Jensen, J. B., and Gras, J. L.: Soot particles in the free troposphere over Australia, Atmos. Environ., 39, 5079–5089, https://doi.org/10.1016/j.atmosenv.2005.05.015, 2005.

Ouf, F. X., Bourrous, S., Vallières, C., Yon, J., and Lintis, L.: Specific surface area of combustion emitted particles: Impact of primary particle diameter and organic content, J. Aerosol Sci., 137, 105436, https://doi.org/10.1016/j.jaerosci.2019.105436, 2019.

Pei, X., Hallquist, M., Eriksson, A. C., Pagels, J., Donahue, N. M., Mentel, T., Svenningsson, B., Brune, W., and Pathak, R. K.: Morphological transformation of soot: investigation of microphysical processes during the condensation of sulfuric acid and limonene ozonolysis product vapors, Atmos. Chem. Phys., 18, 9845–9860, https://doi.org/10.5194/acp-18-9845-2018, 2018.

Persiantseva, N. M., Popovicheva, O. B., and Shonija, N. K.: Wetting and hydration of insoluble soot particles in the upper troposphere, J. Environ. Monit., 6, 939–945, https://doi.org/10.1039/b407770a, 2004.

Petzold, A. and Schröder, F. P.: Jet engine exhaust aerosol characterization, Aerosol Sci. Tech., 28, 62–76, https://doi.org/10.1080/02786829808965512, 1998.

Petzold, A., Strom, J., Ohlsson, S., and Schröder, F. P.: Elemental composition and morphology of ice-crystal residual particles in cirrus clouds and contrails, Atmos. Res., 49, 21–34, https://doi.org/10.1016/S0169-8095(97)00083-5, 1998.

Popovicheva, O. B., Persiantseva, N. M., Lukhovitskaya, E. E., Shonija, N. K., Zubareva, N. A., Demirdjian, B., Ferry, D., and Suzanne, J.: Aircraft engine soot as contrail nuclei, Geophys. Res. Lett., 31, L11104, https://doi.org/10.1029/2003gl018888, 2004.

Popovicheva, O. B., Persiantseva, N. M., Shonija, N. K., DeMott, P., Koehler, K., Petters, M., Kreidenweis, S., Tishkova, V., Demirdjian, B., and Suzanne, J.: Water interaction with hydrophobic and hydrophilic soot particles, Phys. Chem. Chem. Phys., 10, 2332–2344, https://doi.org/10.1039/b718944n, 2008a.

Popovicheva, O. B., Persiantseva, N. M., Tishkova, V., Shonija, N. K., and Zubareva, N. A.: Quantification of water uptake by soot particles, Environ. Res. Lett., 3, 025009, https://doi.org/10.1088/1748-9326/3/2/025009, 2008b.

Pósfai, M., Anderson, J. R., Buseck, P. R., and Sievering, H.: Soot and sulfate aerosol particles in the remote marine troposphere, J. Geophys. Res.-Atmos., 104, 21685–21693, https://doi.org/10.1029/1999jd900208, 1999.

Pye, H. O. T., Nenes, A., Alexander, B., Ault, A. P., Barth, M. C., Clegg, S. L., Collett Jr, J. L., Fahey, K. M., Hennigan, C. J., Herrmann, H., Kanakidou, M., Kelly, J. T., Ku, I. T., McNeill, V. F., Riemer, N., Schaefer, T., Shi, G., Tilgner, A., Walker, J. T., Wang, T., Weber, R., Xing, J., Zaveri, R. A., and Zuend, A.: The acidity of atmospheric particles and clouds, Atmos. Chem. Phys., 20, 4809–4888, https://doi.org/10.5194/acp-20-4809-2020, 2020.

Saathoff, H., Naumann, K. H., Schnaiter, M., Schöck, W., Möhler, O., Schurath, U., Weingartner, E., Gysel, M., and Baltensperger, U.: Coating of soot and $(NH_4)_2SO_4$ particles by ozonolysis products of α-pinene, J. Aerosol Sci., 34, 1297–1321, https://doi.org/10.1016/s0021-8502(03)00364-1, 2003.

Schill, G. P. and Tolbert, M. A.: Depositional ice nucleation on monocarboxylic acids: effect of the O:C ratio, J. Chem. Phys. A, 116, 6817–6822, https://doi.org/10.1021/jp301772q, 2012.

Schnitzler, E. G., Gac, J. M., and Jäger, W.: Coating surface tension dependence of soot aggregate restructuring, J. Aerosol Sci., 106, 43–55, https://doi.org/10.1016/j.jaerosci.2017.01.005, 2017.

Shen, Z., Liu, J., Horowitz, L. W., Henze, D. K., Fan, S., H, L., II, Mauzerall, D. L., Lin, J. T., and Tao, S.: Analysis of transpacific transport of black carbon during HIPPO-3: implications for black carbon aging, Atmos. Chem. Phys., 14, 6315–6327, https://doi.org/10.5194/acp-14-6315-2014, 2014.

Takemura, T. and Suzuki, K.: Weak global warming mitigation by reducing black carbon emissions, Sci. Rep., 9, 4419, https://doi.org/10.1038/s41598-019-41181-6, 2019.

Thommes, M., Kaneko, K., Neimark, A. V., Olivier, J. P., Rodriguez-Reinoso, F., Rouquerol, J., and Sing, K. S. W.: Physisorption of gases, with special reference to the evaluation of surface area and pore size distribution (IUPAC Technical Report), Pure Appl. Chem., 87, 1051–1069, https://doi.org/10.1515/pac-2014-1117, 2015.

Tritscher, T., Jurányi, Z., Martin, M., Chirico, R., Gysel, M., Heringa, M. F., DeCarlo, P. F., Sierau, B., Prévôt, A. S. H., Weingartner, E., and Baltensperger, U.: Changes of hygroscopicity and morphology during ageing of diesel soot, Environ. Res. Lett., 6, 034026, https://doi.org/10.1088/1748-9326/6/3/034026, 2011.

Twohy, C. H. and Poellot, M. R.: Chemical characteristics of ice residual nuclei in anvil cirrus clouds: evidence for homogeneous and heterogeneous ice formation, Atmos. Chem. Phys., 5, 2289–2297, https://doi.org/10.5194/acp-5-2289-2005, 2005.

Vali, G., DeMott, P. J., Möhler, O., and Whale, T. F.: Technical Note: A proposal for ice nucleation terminology, Atmos. Chem. Phys., 15, 10263–10270, https://doi.org/10.5194/acp-15-10263-2015, 2015.

Vander Wal, R. L., Yezerets, A., Currier, N. W., Kim, D. H., and Wang, C. M.: HRTEM Study of diesel soot collected from diesel particulate filters, Carbon, 45, 70–77, https://doi.org/10.1016/j.carbon.2006.08.005, 2007.

Virtanen, A., Joutsensaari, J., Koop, T., Kannosto, J., Yli-Pirila, P., Leskinen, J., Makela, J. M., Holopainen, J. K., Poschl, U., Kulmala, M., Worsnop, D. R., and Laaksonen, A.: An amorphous solid state of biogenic secondary organic aerosol particles, Nature, 467, 824–827, https://doi.org/10.1038/nature09455, 2010.

Whale, T. F., Rosillo-Lopez, M., Murray, B. J., and Salzmann, C. G.: Ice Nucleation Properties of Oxidized Carbon Nanomaterials, J. Phys. Chem. Lett., 6, 3012–3016, https://doi.org/10.1021/acs.jpclett.5b01096, 2015.

Wyslouzil, B. E., Carleton, K. L., Sonnenfroh, D. M., Rawlin, W. T., and Arnold, S.: Observation of hydration of single, modified carbon aerosols, Geophys. Res. Lett., 21, 2107–2110, 1994.

Xue, H., Lu, Y., Geng, H., Dong, B., Wu, S., Fan, Q., Zhang, Z., Li, X., Zhou, X., and Wang, J.: Hydroxyl Groups on the Graphene Surfaces Facilitate Ice Nucleation, J. Phys. Chem. Lett., 10, 2458–2462, https://doi.org/10.1021/acs.jpclett.9b01033, 2019.

Zhang, C., Zhang, Y., Wolf, M. J., Nichman, L., Shen, C., Onasch, T. B., Chen, L., and Cziczo, D. J.: The effects of morphology, mobility size, and secondary organic aerosol (SOA) material coating on the ice nucleation activity of black carbon in the cirrus regime, Atmos. Chem. Phys., 20, 13957–13984, https://doi.org/10.5194/acp-20-13957-2020, 2020.

Zhang, D. and Zhang, R.: Laboratory Investigation of Heterogeneous Interaction of Sulfuric Acid with Soot, Environ. Sci. Technol., 39, 5722–5728, 2005.

Zhang, R., Khalizov, A. F., Pagels, J., Zhang, D., Xue, H., and McMurry, P. H.: Variability in morphology, hygroscopicity, and optical properties of soot aerosols during atmospheric processing, P. Natl. Acad. Sci. USA, 105, 10291–10296, 2008.

Zhang, X., Karl, M., Zhang, L., and Wang, J.: Influence of Aviation Emission on the Particle Number Concentration near Zurich Airport, Environ. Sci. Technol., 54, 14161–14171, https://doi.org/10.1021/acs.est.0c02249, 2020.